TWINNING MECHANISMS IN NON-MODULATED NI-MN-GA

By

Brittany Rana Muntifering

A thesis

submitted in partial fulfillment

of the requirements for the degree of

Master of Science in Materials Science & Engineering

Boise State University

August 2011

BOISE STATE UNIVERSITY GRADUATE COLLEGE

DEFENSE COMMITTEE AND FINAL READING APPROVALS

of the thesis submitted by

Brittany Rana Muntifering

Thesis Title: Twinning Mechanisms in Non-Modulated Ni-Mn-Ga

Date of Final Oral Examination: 21 June 2011

The following individuals read and discussed the thesis submitted by student Brittany Rana Muntifering, and they evaluated her presentation and response to questions during the final oral examination. They found that the student passed the final oral examination.

Peter Müllner, Ph.D.	Chair, Supervisory Committee
Rick Ubic, Ph.D.	Member, Supervisory Committee
Robert C. Pond, Ph.D.	Member, Supervisory Committee

The final reading approval of the thesis was granted by Peter Müllner, Ph.D., Chair of the Supervisory Committee. The thesis was approved for the Graduate College by John R. Pelton, Ph.D., Dean of the Graduate College.

ACKNOWLEDGEMENTS

It is difficult to overstate my gratitude to my advisor, Dr. Peter Müllner, for his enthusiasm, motivation, patience, and his great efforts to explain things clearly and simply. I would also like to thank Dr. Bob Pond for his expertise and guidance throughout the project, as well as Dr. Rick Ubic for his guidance with the TEM and experimental techniques.

The members of the Müllner group have contributed immensely to my personal and professional time at Boise State. The group has been a source of friendships as well as good advice, insightful discussions, and collaboration. I would like to express my gratitude to Kimo Wilson, Nikki Kucza, Doug Kellis, Cassie Witherspoon, Adrian Rothenbuhler, Dr. Paul Lindquist, Martika Flores, Brittany Siewert, Kimball Anderson, Dr. Kari Ullakko, Courtney Hollar, Aaron Smith, Ken McDonald, Dave Shenker, Markus Chmielus, and all the others who have spent time working with me. I am especially grateful to Steve Letourneau for his assistance learning the TEM and microscopy techniques. I would also like to thank the entire faculty and staff in the Materials Science and Engineering department for being phenomenal educators.

Finally, I would like to thank my family for always supporting me and stressing the value of continued educated.

Financial and technical support for the research in this thesis was provided by the National Science Foundation and the Department of Energy.

ABSTRACT

The reversible magnetic-field-induced plastic deformation that occurs in Ni-Mn-Ga alloys proceeds through the field-induced displacement of twin boundaries in the martensite phase. On the microscopic scale, the twin boundaries move through the motion of twinning dislocations. A fundamental understanding of the motion of twin boundaries requires detailed characterization of the twinning systems and the associated twinning dislocations. Twinning dislocations and twin microstructure of non-modulated Ni-Mn-Ga martensite were characterized with transmission electron microscopy. For ease of interpreting results, two different axis systems were used to represent the non-modulated structure: a face-centered tetragonal (T) lattice and a body-centered monoclinic (2M) lattice.

Two types of martensite variant interfaces were studied. The habit plane of the twins within each variant is $(001)_{2M}/(101)_T$. One type of interface appears smooth, where the martensite variants themselves are related with the habit plane $(\bar{1}21)_{2M}/(022)_T$. A second type of interfaces appears stepped, with a microscopic habit plane $(100)_{2M}$ / $(10\bar{1})_T$. Close to an inter-variant martensite interface, the thickness of twins varies. This is explained in terms of twin branching. It is shown that the modulated martensite structures can be constructed from branching of the non-modulated structure into nano-twinned variants.

Off-axis imaging of twins produced a distinct fringe pattern. Three fringe contrast levels appeared in a repeating sequence. The repeating contrast is consistent with a twin produced by an array of twinning dislocations with Burgers vector $\frac{1}{6}[100]_{2M} / \frac{1}{12}[10\bar{1}]_{T}$ and a step height equal to the d spacing of the $(001)_{2M}/(101)_{T}$ planes.

TABLE OF CONTENTS

LIST OF TABLES

LIST OF FIGURES

CHAPTER 1: INTRODUCTION

Shape-memory alloys (SMAs) are a class of functional materials that have the unique ability to recover from large strains without permanent deformation [1]. Thermally activated SMAs, such as NiTi, exhibit linear plastic deformations of up to 6%. This deformation is recoverable by heating the deformed martensite through the martensitic transformation temperature. Upon heating, the material "remembers" and returns to its original, cold-forged or trained shape [1, 2].

It was speculated for years that the large strains associated with the thermoelastic shape-memory effect, such as in NiTi alloys, could be captured by the application of a magnetic field in certain martensites that are also ferromagnetic [3]. This speculation was proven correct in 1996 when Ullakko and coworkers reported 0.2% magnetic-field-induced strain (MFIS) in single crystals of Ni-Mn-Ga [4]. The MFIS recorded in Ni-Mn-Ga single crystals increased to 6% in 2000 [5] and 9.6% in 2002 by varying the composition and martensite variant selection [6-8].

Magnetic shape memory alloys (MSMAs) deform, changing shape and dimensions, under the application of an externally applied magnetic field; however, unlike conventional SMAs that must thermally proceed through a martensitic transformation, the strains in MSMAs can be recovered by the rotation of the magnetic field [4, 6, 7, 9, 10]. MSMAs have an advantage over conventional shape memory alloys due to the much higher frequency range over which they can be operated, exceeding

1 kHz. The actuation in MSMAs is driven by magnetic-field-induced reorientation of martensitic variants and is not limited by heat transfer as it is for traditional SMAs [11]. The recoverable strain seen in Ni-Mn-Ga alloys (up to 10%) is two orders of magnitude larger than the magnetic-field-induced strain observed in ordinary magnetostrictive materials, such as Terfenol-D, which has shown strain of 0.24% [11], and is also much larger than the electric field induced strain in piezoelectrics, which can strain up to 0.1% [12].

The Ni-Mn-Ga alloy has potential for numerous applications including actuators, sensors, and power generators [13-15]. Due to their unique magneto-mechanical properties and numerous potential applications, magnetic shape memory alloys, specifically Ni-Mn-Ga alloys, have recently attracted significant interest from the scientific community.

CHAPTER 2: MOTIVATION

The macroscopically observable magnetic-field-induced strain in MSMAs is caused by the reorientation of martensitic variants, or twins [16]. For MFIS to occur, it is necessary that the magnetic anisotropy of the martensite phase be large compared to the energy required for twin boundary motion. It is also required that the preferred direction of magnetization change across the twin boundary. When this is the case, application of a magnetic field results in a difference in Zeeman energy across the twin boundary. This energy difference exerts a pressure on the twin boundary so as to grow the twin variant having the more favorable orientation [5, 9, 17]. The resulting field-induced twin-boundary motion produces a large strain, fully within the martensitic state of an MSMA.

On the microscopic scale, twins grow and shrink by the movement of dislocations located in steps of the twin boundary [18-20]. A defect with both a dislocation and step character is called a disconnection [19, 20]. Disconnections can be driven to move along twin boundaries by an internal stress such as that caused by a magnetic field. This results in a displacement of the twin boundary whereby one twin domain grows while the adjacent domain shrinks. In addition, the dislocation character produces a deformation by shearing the two crystals with respect to each other [21].

To develop MSMAs into applications, it is important to be able to systematically and reproducibly influence the properties of MSMAs and to predict these properties accurately. The effects of microstructure, particularly disconnections, on the magnetic-

field-induced strain are not yet fully understood and an understanding of the character of the disconnections that play a role in the magnetic-shape-memory effect is currently lacking. A fundamental understanding of the motion of twin boundaries requires a detailed characterization of these twinning dislocations.

The objective of the present work is to study the microstructure of the non-modulated martensite. Specifically, a complete and consistent description of the crystal structure of the non-modulated martensite, the twinning systems present, and the types of defects present in the twin interfaces was developed. The relation between the non-modulated structure and the more complicated modulated structures was also considered.

CHAPTER 3: BACKGROUND

The following chapter provides an overview of the basic mechanisms of twinning and the types of defects associated with twin boundaries. Section 3.1 discusses the crystallography of twinning and the concepts of hierarchical twinning and twin branching. An overview of defects including twinning dislocations, disconnections, and disclinations is also presented. Section 3.2 discusses the most common crystal structures seen in the Ni-Mn-Ga alloy, including the austenite and martensite structures. An overview of martensitic transformations is also presented. Section 3.3 presents the concept of magnetoplasticity in magnetic-shape-memory alloys in terms of twin boundary motion.

3.1 Twinning

3.1.1 Crystallography of Twinning

Deformation twinning is a process in which a region of a crystal undergoes a homogeneous shear that produces the original crystal structure in a new orientation [22]. In the simplest case, this results in the atoms of the original crystal, ‘parent’, and those of the product crystal, ‘twin’, being mirror images of each other by reflection over the twinning plane. This is seen schematically in Figure 3.1, where the matrix crystal (purple) is reflected over the twin boundary (TB) to produce the twin (blue). The black atoms along the twin boundary are shared by both the matrix and the twin.

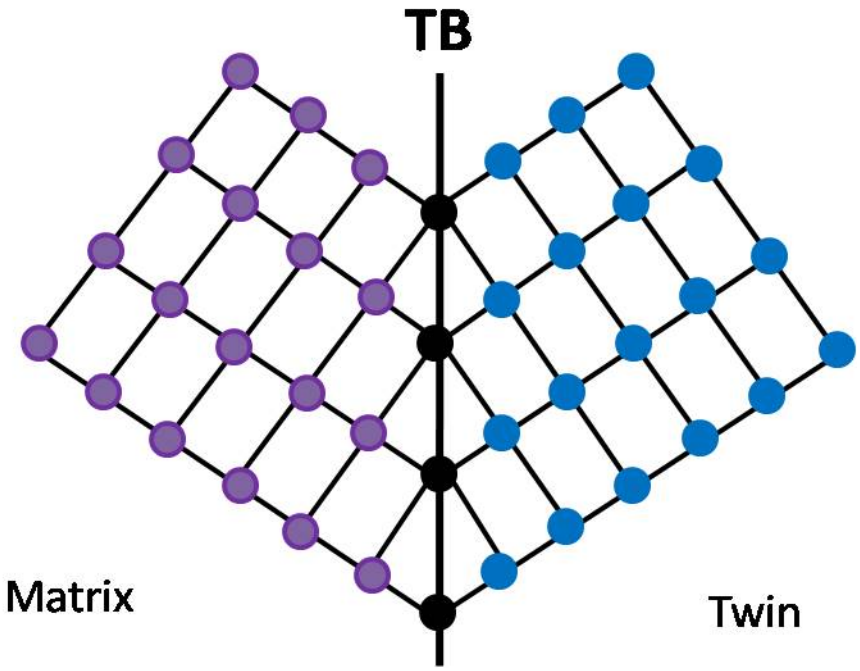

Figure 3.1 Diagram Showing the Matrix Structure (Purple), and the Twin (Blue), Which Is a Result of a Mirror Reflection of the Matrix Crystal Structure Over the Twin Boundary (TB).

The twinning elements are shown schematically in Figure 3.2. The plane parallel to the large twin interface, called the habit plane, remains undistorted, and is denoted K_1. The shear direction is denoted η_1. The plane K_2, which intersects K_1 in a line perpendicular to the shear direction, and which makes equal angles with K_1 before and after the shear, is also undistorted. The plane of shear, s, is the plane that is normal to K_1 and contains η_1. The direction η_2 lies along the line of intersection of the shear plane and K_2 [22, 23].

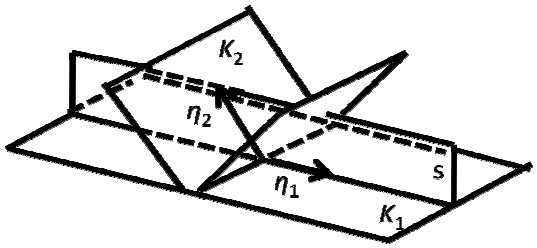

Figure 3.2 Illustration of the Twinning Elements: η_1 Lying in K_1, η_2 Lying in K_2, and the Shear Plane s, Perpendicular to K_1 and K_2 and Containing η_1 and η_2. The Sheared Position of K_2 After a Shear η_1 on K_1 Is Also Shown.

The requirement that the crystal lattice not be changed by the shear leads to the condition that either K_1 and η_2 both have rational, low index indices (type I twin) or K_2 and η_1 both have rational, low-index indices (type II twin) [24, 25]. If all four indices are rational, the twin is called a compound twin.

3.1.2 Hierarchical Twinning

In "hierarchically" twinned microstructures, secondary twins form within primary twins, tertiary twins form within secondary twins, etc. Higher-order twins form within lower-order twins, and higher-order twins are smaller than lower-order twins [26, 27]. This effect is seen in $(Ni_{51}Mn_{28}Ga_{21})_{99.5}Dy_{0.5}$ in Figure 3.3, which shows three levels of twinning [28]. The smallest level of twins are indicated by red lines, the second level by blue lines, and the largest twins are indicated by green lines.

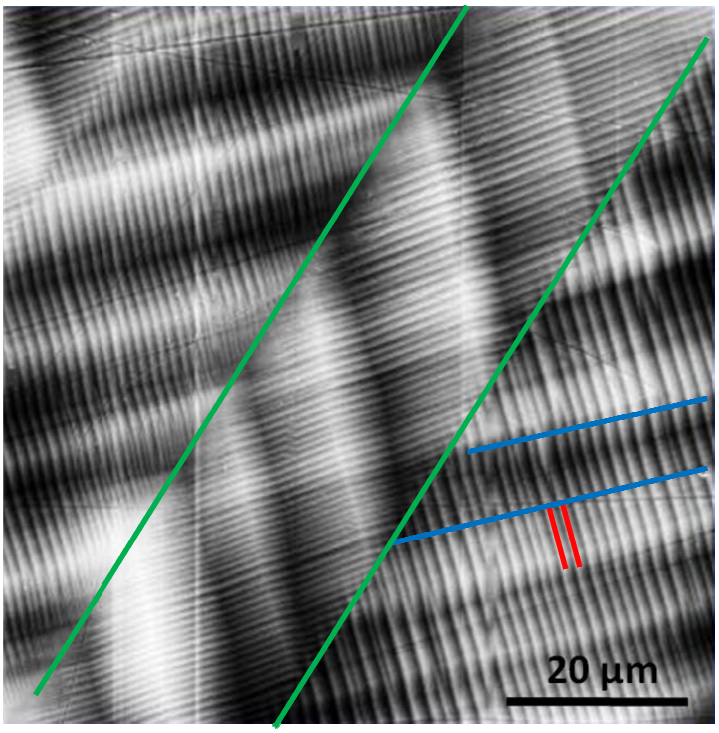

Figure 3.3 Hierarchical Twinning in $(Ni_{51}Mn_{28}Ga_{21})_{99.5}Dy_{0.5}$. Three Levels of Twinning Are Indicated by Green (Primary), Blue (Secondary), and Red (Tertiary). Reprinted with Kind Permission from [28].

When secondary twins are present, the habit plane of the primary twin can be distorted and, therefore, will not be strain-free [27]. Another plane will then become the habit plane of the structured twin. The secondary twins impose a rotation or misorientation in the primary twin, which is proportional to the fraction of secondary twins present. There is an in-plane distortion along the interface of the structured twin, resulting in rotation of the habit plane. The deformation of a hierarchically twinned martensite structure via twinning requires that twin boundaries move in a coordinated and collective way [26].

3.1.3 Twin Branching

Kohn and Müller examined the minimization of the total energy, consisting of elastic and interfacial energy, in the context of an austenite-twinned-martensite interface [29]. Two solutions were found, corresponding to two distinct regimes. The first regime was one in which the twin width, W, is related to twin length, L, by

$$W \propto \rho^{1/2} L^{1/2} \tag{1}$$

where ρ is a materials constant with dimensions of length. This corresponds to an austenite phase that is sufficiently 'soft' in shear and/or the surface energy of the twin interfaces is sufficiently large.

The second regime is one in which the twins branch as they approach the austenite interface. At distance l, the twin width behaves as

$$W \propto \rho^{1/3} l^{2/3} \tag{2}$$

This type of behavior occurs because elastic energy minimization prefers fine twins at the austenite-twinned-martensite interface. Far from the austenite, there is no elastic advantage to the fine-scale structure. Instead, fine twins actually cost surface energy, which results in twin coarsening. The result of a simulation of branched twin structure at an austenite interface is seen in Figure 3.4 [29].

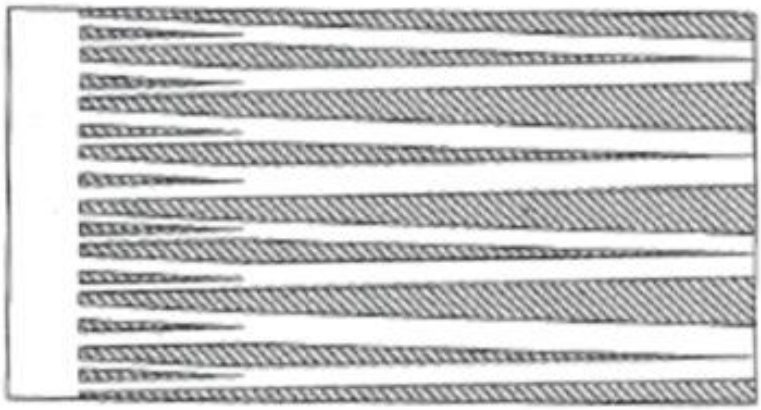

Figure 3.4 Simulated Austenite/Twinned-Martensite Interface. Twins Were Seen to Branch Close to the Austenite Inferface Because Elastic Energy Minimization Prefers Fine Twins at the Interface, While Far from the Interface Twins Coarsen to Reduce Surface Energy. Reprinted with Kind Permission from [29].

3.1.4 Twinning Dislocations

Frank and van der Merwe [30] reported that a step on a coherent twinning plane would cause several severely distorted unit cells in the center of the step. This distortion was noted to contain a dislocation with a Burgers vector that is not a full lattice vector. Such a dislocation is called a partial dislocation. The authors referred to this defect as a 'twinning dislocation'. The Burgers vector is parallel to the twinning plane, which coincides with the glide plane of the dislocation. It was predicted that the defect "should by its motion translate the twinning surface, causing one twin to grow into the other: and an applied stress should cause it to move." The original image published by Frank and van der Merwe is reproduced in Figure 3.5, where the distorted unit cells around the step can be seen.

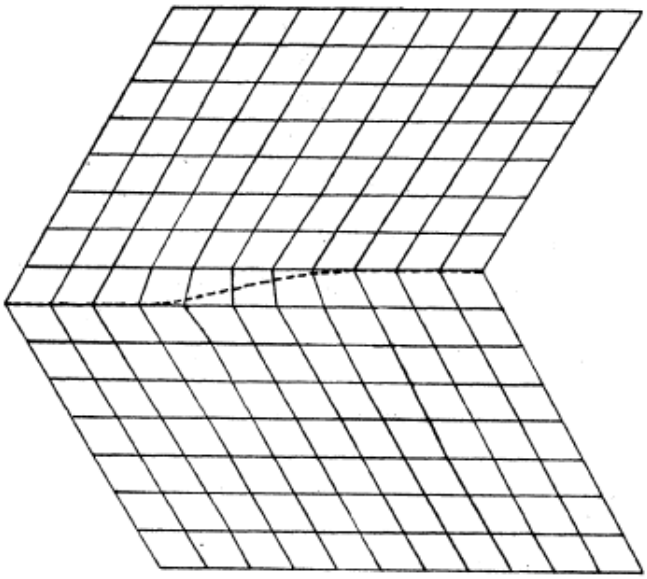

Figure 3.5 Schematic of a Coherent Twin Interface with a Step Introduced in the Center. The Unit Cells in the Vicinity of the Step Are Distorted. This Distortion Contains a Partial Dislocation. This Type of Defect Was Termed 'Twinning Dislocation'. Reprinted with Kind Permission from [30].

Using this model of twining dislocations, it was shown that the shear of a portion of a crystal into a twin can be accomplished by the successive motion of twinning dislocations, each on a glide plane one inter planar spacing removed from its predecessor. The twinning dislocations can move conservatively along the twin boundary without requiring diffusion. The tip of an advancing twin therefore corresponds to a dislocation pileup [22]. This is shown schematically in Figure 3.6, where a twin is advancing into the matrix. The twin grows by the motion of twinning dislocations on successive steps in the twin.

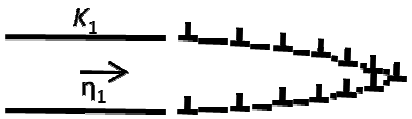

Figure 3.6 Schematic Showing a Twin Advancing into the Matrix. The Twin Is Formed by Dislocations with Burgers Vectors Parallel to η_1 Gliding on K_1. Reprinted with Kind Permission from [22].

3.1.5 Twinning Disconnections

Hirth and Pond [20] developed a theory of moving crystal interfaces based on interfacial line defects, which they call 'disconnections'. Conventionally, the two crystals are labeled μ and λ (black and white). If a bicrystal is created by bringing the upper planar surface of μ, with outward planar normal vector **n,** into contact with a lower planar surface of λ, as seen in Figure 3.7, a defect-free interface can result.

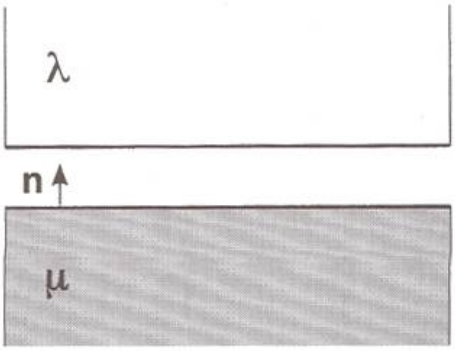

Figure 3.7 Illustration of the Formation of a Defect Free Bicrystal by Joining Planar Surfaces of Crystals λ and μ. Reprinted with Kind Permission from [31].

If the surface of μ and/or λ contains a step and the surface structure is identical on either side of the step, the step must be related to the crystal symmetry. It can be characterized by a translation vector, $\mathbf{t}_i$ (i=μ,λ), of the lattice. The height, h_i, of such a step is

$$h_i = \mathbf{n}\cdot\mathbf{t} \tag{3}$$

The step height can be signed positive or negative. If the surfaces with steps are brought together to form a bicrystal with no atoms removed and no spaces left along the stepped interface, the material in the vicinity of the resulting overlap step will have to be distorted to fit. Thus, a dislocation is created with Burgers vector

$$\mathbf{b} = \mathbf{t}_\lambda - \mathbf{t}_\mu \tag{4}$$

If two surfaces have steps with height of opposite sign, the resultant interface defect is a dislocation with no step character. This is illustrated in Figure 3.8, where $h_\lambda = -h_\mu$.

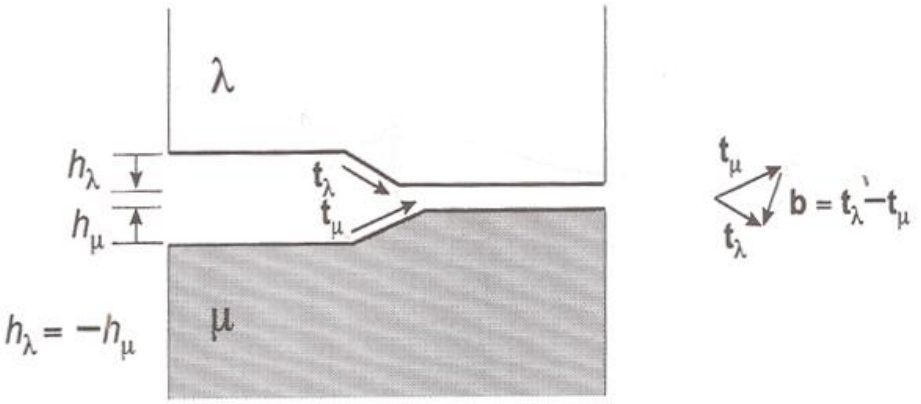

Figure 3.8 Illustration of the Formation of a Bicrystal by Joining Surfaces of Crystals λ and μ. The Crystals Have Heights of Equal but Opposite Value. This Results in a Defect of Pure Dislocation Character, Where $\mathbf{b} = \mathbf{t}_\lambda - \mathbf{t}_\mu$. Reprinted with Kind Permission from [31].

If crystals are joined in which the translation vectors are equal ($\mathbf{t}_\lambda = \mathbf{t}_\mu$ /$h_\lambda = h_\mu$), then the defect is pure step without dislocation character. This type of defect is shown in Figure 3.9.

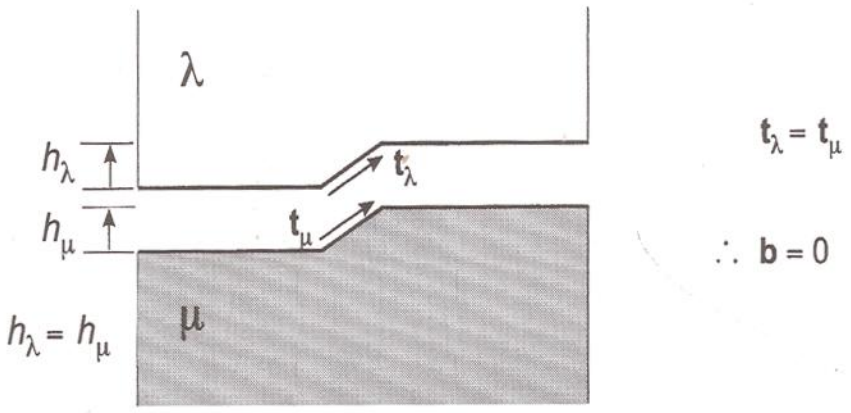

Figure 3.9 Illustration of the Formation of a Bicrystal by Joining Surfaces of Crystals λ and μ. The Crystals Have Translation Vectors Which Are Equal in Value. The Step Heights Are of Equal Value. This Results in a Defect of Pure Step Character, Where b = 0. Reprinted with Kind Permission from [31].

If the surfaces have steps with heights that are of the same sign but **t** vectors that are not equal, the interface will have both a step height and Burgers vector. These types of defects are termed disconnections. The step height, *h*, is equal to the height of smaller magnitude (h_λ or h_μ). This type of defect is illustrated in Figure 3.10.

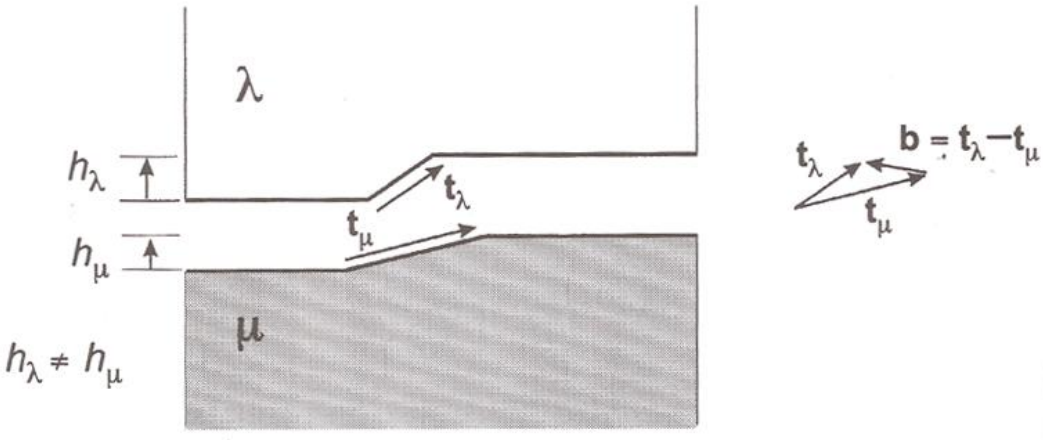

Figure 3.10 Illustration of the Formation of a Bicrystal by Joining Surfaces of Crystals λ and μ. The Crystals Have Different Step Heights and Non-Parallel Translation Vectors. This Results in a Defect Which Has Both Step and Dislocation Character, Called a Disconnection. $b = t_\lambda - t_\mu$ and the Step Height Is Equal to the Smaller of h_λ and h_μ. Reprinted with Kind Permission from [31].

A special type of disconnection is one in which $h_\lambda = h_\mu = h$, but the translation vectors are not parallel. The Burgers vector of this type of disconnection has no component perpendicular to the interface and it is free to glide along the interface. A special case of this type of disconnection is a twinning dislocation, as discussed in Section 3.1.4.

Disconnections play an important role in phase transformations involving the growth of one crystal at the expense of the other. Examples include twinning, martensitic transformations (see Section 3.2.2), and precipitation [19]. The motion of disconnections over the interface is the mechanism that transforms sites of one crystal to sites of the other.

Disconnections that have a small Burgers vector and step height and move in a glissile manner with minimal atomic shuffling are likely to be mobile [19]. Defects having a relatively large Burgers vector may decompose into "partial disconnections." For partial disconnections, the interface structures on either side of the disconnection are not identical. For twining dislocations, wider cores lead to enhanced mobility. A larger step height tends to localize a defect's core and motion generally requires extensive shuffling.

3.1.6 Twinning Disclinations

A disclination is a linear defect that bounds the surface of a cut in a continuous body, with the undeformed faces of the cut undergoing the displacement produced by mutual rotation around a fixed axis. The rotation is defined by a rotation axis and a rotation angle ω (also called disclination strength) [32, 33]. Material is removed where it overlaps and inserted where there is a gap. The rotation axis may have any orientation

and position relative to the cylinder axis. Figure 3.11 demonstrates three different methods of formation of a disclination. Figure 3.11 (a) and (b) show twist disclinations in which the rotation axis is perpendicular to the cylinder axis. Figure 3.11 (c) shows a wedge disclination in which the rotation axis coincides with the cylinder axis.

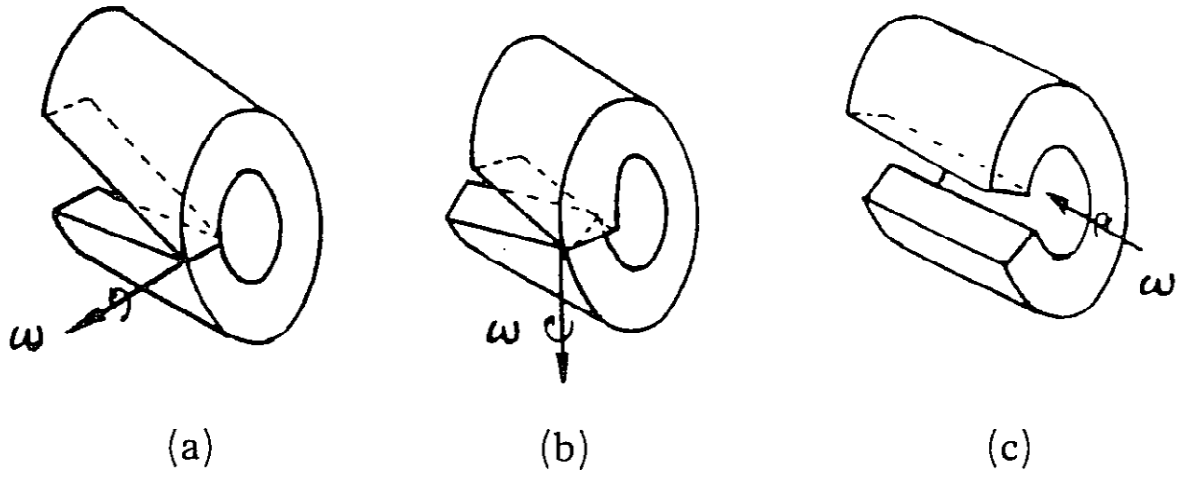

Figure 3.11 Disclination Formation in a Cylinder. A Cut Is Made in the Cylinder and the Faces Are Rotated About ω. (a) and (b) Show Twist Disclinations in Which the Rotation Axis Is Perpendicular to the Cylinder Axis. (c) Shows a Wedge Disclination in Which the Axis of Rotation Is Parallel to the Cylinder Axis. Reprinted with Kind Permission from [33].

Figure 3.12 (a)-(f) shows the disclination projected along its line. The surfaces of the cut are rotated with respect to each other such that a wedge-shaped gap is formed (Figure 3.12 (a)). A wedge-shaped piece exactly matching the gap is inserted in Figure 3.12 (b) and the interfaces are adhered in Figure 3.12(c). This forms a negative wedge disclination, which is symbolized by an open triangle in Figure 3.12(c). A positive wedge disclination, symbolized by a solid triangle, is formed when the rotation produces overlapping material that needs to be removed, as in Figures 3.12 (d)-(f).

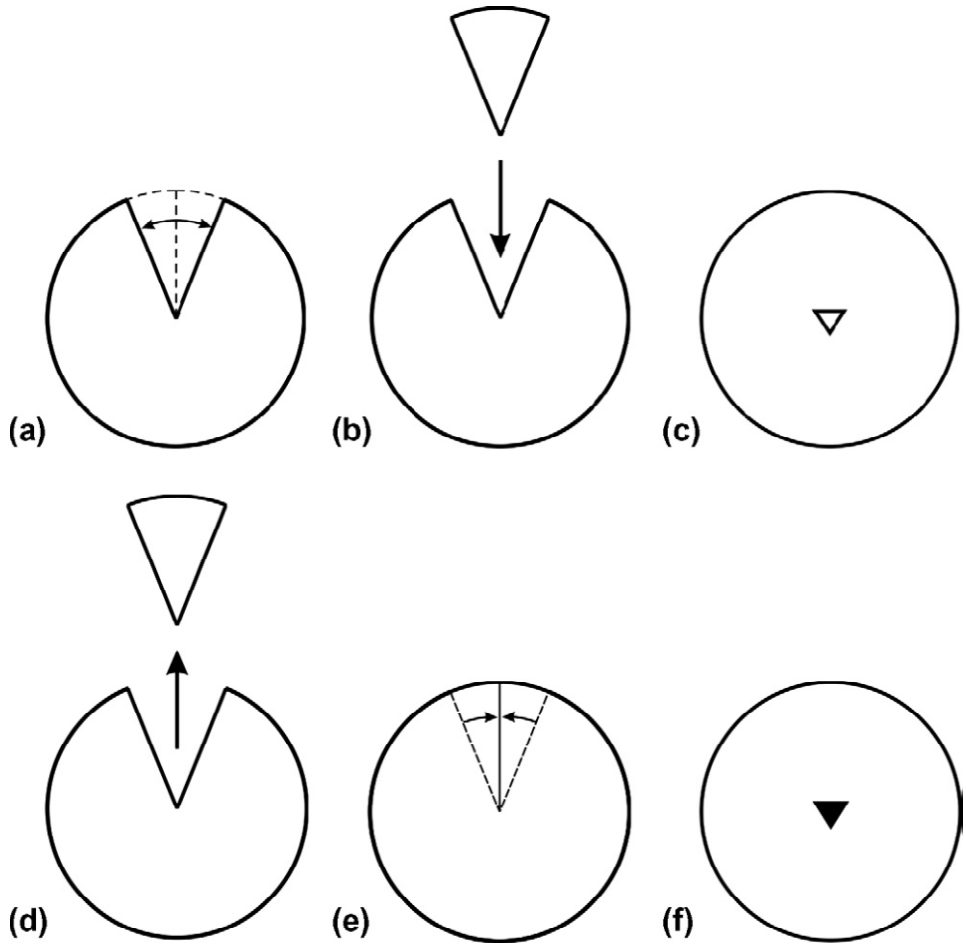

Figure 3.12 Schematic Demonstrating the Formation of Positive and Negative Wedge Disclinations. Material Is Inserted (a–c) to Form the Negative Wedge Disclination (Open Triangle) and Removed (d-f) to Form a Positive Wedge Disclination (Filled Triangle). Reprinted with Kind Permission from [26].

There is a direct relationship between disclinations and dislocations. Any disclination can be represented in the form of a super-position of dislocations. Likewise, any dislocation can be represented by a set of disclinations [33]. For example, two parallel disclinations at a distance $2a$, one positive, with strength ω, the other negative, with strength $-\omega$, form a disclination dipole. The long-range stress field of a wedge disclination dipole is the same as that of an edge dislocation [26] with Burgers vector

$$b = 2a\omega \tag{5}$$

The wedge-shaped gap may be approximated by crystal surfaces with step height *h* and step width **b**/2 [26] (Figure 3.13). If a wedge with complementary steps is inserted, as in Figure 3.13(b), a wall of dislocations is formed with Burgers vector **b** and dislocation separation *h* (Figure 3.13(c)). Figures 3.13 (d)-(f) show the dislocation approximation when material is removed.

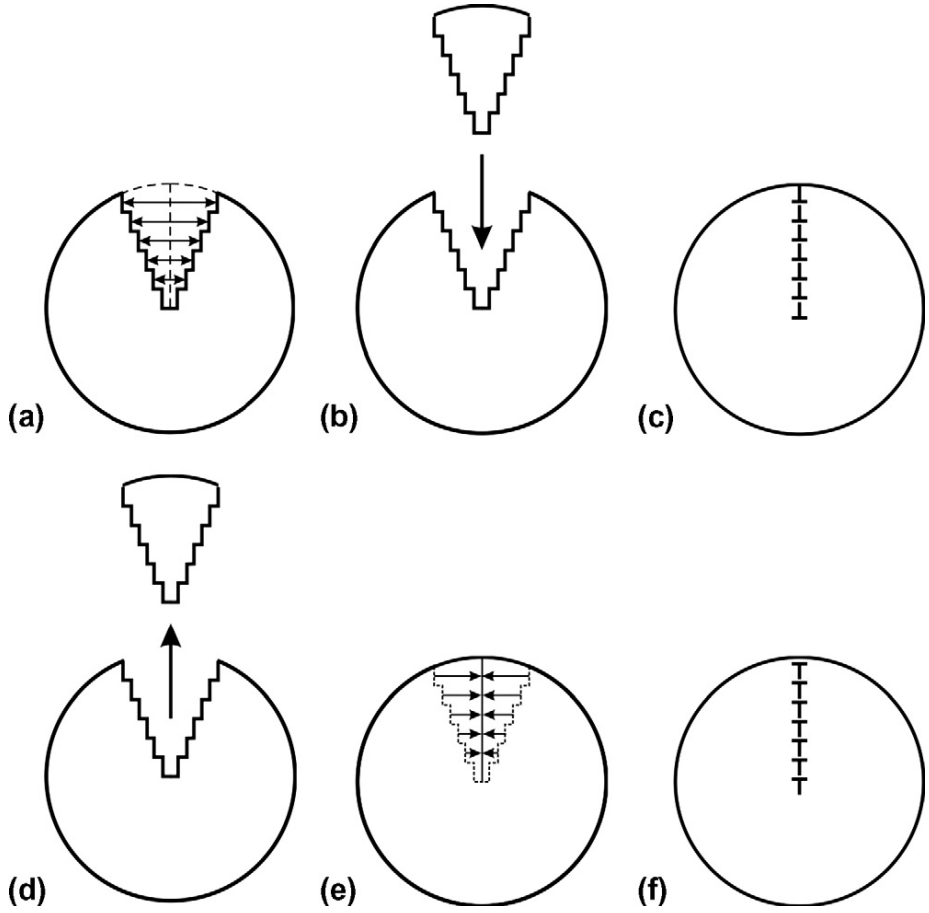

Figure 3.13 The Wedge-Shaped Gap May Be Approximated By Crystal Surfaces with Step Height h and Step Width b/2 [26]. (b) A Wedge with Complementary Steps Is Inserted, Creating a Wall of Dislocations with Burgers Vector b and Dislocation Separation h. (d-f) Dislocation Approximation When Material Is Removed. Reprinted with Kind Permission from [26].

When the step width and step height are reduced with constant ratio, b/h, until they are infinitesimal, a wedge disclination is obtained [26] with strength

$$\omega = b/h \tag{6}$$

Therefore, a disclination is equivalent to a semi-infinite wall of infinitesimal dislocations. A disclination dipole can be represented by different dislocation arrangements as seen in Figure 3.14 (a)-(e). Each disclination corresponds to a semi-infinite wall of edge dislocations. The two walls may be extended to the left side (Figure 3.14 (b)), to the right side (Figure 3.14 (c)), or to the top or bottom (Figure 3.14 (d)). In the case of Figure 3.14 (d), the dislocation walls overlap and most of their dislocations mutually cancel because they have opposite sign. Therefore, the net dislocation wall is finite. The finite dislocation wall has a finite net Burgers vector and may be considered a super dislocation, shown in Figure 3.14 (e). Which defect arrangement describes the physical situation best depends on the nature of the atomic arrangement, the crystallography, the length scale, and the accuracy required of the model [26].

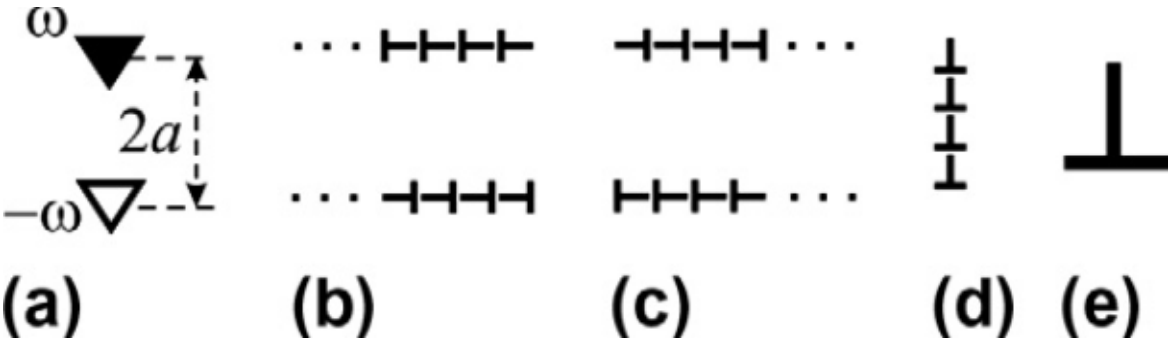

Figure 3.14 a) Various Dislocation Representations for a Disclination Dipole. b) and c) Pairs of Semi-Infinite Dislocation Walls, d) A Finite Dislocation Wall. e) A Superdislocation. Reprinted with Kind Permission from [26].

When moving as dipoles, disclinations produce a homogeneous shear in the volume bound by the glide planes of each disclination. The shear ratio, *s*, is related to the strength of the disclination by

$$s = 2\tan\frac{\omega}{2} \approx \omega \tag{7}$$

The strength, ω, of the twinning disclination is related to the Burgers vector and the step height of the twinning disconnection as

$$\omega = 2\tan^{-1}\frac{b}{2h} \approx s \tag{8}$$

When free to move along an infinite twin boundary, twinning disconnections (described in Section 3.1.5) with like-signed Burgers vectors mutually repel and spread apart as far as they can. Disclinations are formed only where twin boundaries meet other defects such as other twin boundaries, as in hierarchically twinned martensite. For hierarchically twinned martensite, disconnections are attracted towards the lower-order twin boundary where they instantaneously form walls of disclinations with alternating signs, even in the absence of an externally applied stress [28].

3.1.7 Stacking Faults and Twinning

Twinning dislocations were described as partial dislocations located in steps of a coherent twin boundary [30]. Partial dislocations in crystalline material cause stacking faults [22]. A stacking fault is a planar defect and is described as a local region in the crystal where the regular stacking sequence has been interrupted [31].

A common example of a stacking fault is in close-packed structures. Face-centered cubic (fcc) structures differ from hexagonal close packed (hcp) structures only in stacking order. Both structures have close packed atomic planes with six-fold

symmetry. When stacking one of these layers on top of another, the first two layers are identical for hcp and fcc, and labelled AB. If the third layer is placed so that its atoms are directly above those of the first layer, the stacking will be ABA. This is the hcp structure, and it continues ABABABAB; however, there is another location for the third layer, such that its atoms are not above the first layer. Instead, the fourth layer is placed so that its atoms are directly above the first layer. This produces the stacking ABCABCABC, and is actually a cubic arrangement of the atoms. A stacking fault is an interruption in the stacking sequence, for example if the sequence ABCABABCAB were found in an fcc structure.

3.2 Crystal Structures and Martensitic Transformations

3.2.1 Austenite

The high-temperature austenite phase of Ni_2MnGa exhibits an $L2_1$-ordered face centered cubic crystal structure, also known as the Heusler structure [34]. This structure was named after Friedrich Heusler (1866-1947), a German mining engineer and chemist who discovered that upon alloying three non-magnetic metals (Cu, Al, and Mn) the resulting alloy, Cu_2MnAl, is ferromagnetic.

The $L2_1$ structure (space group $Fm\bar{3}m$) has a composition X_2YZ. The X and Y components are generally transition metals. The Y component can also be a rare earth metal. The Z component is a non-metal or non-magnetic metal. In Ni_2MnGa, X, Y, and Z are Ni, Mn, and Ga, respectively. The atomic positions of Ni, Mn, Ga atoms are as follows [34]:

Nickel atoms occupy eight positions at:

[¼ ¼ ¼], [¾ ¼ ¼], [¼ ¾ ¼], [¼ ¼ ¾], [¾ ¾ ¼], [¾ ¼ ¾], [¼ ¾ ¾],

[¾ ¾ ¾]

Manganese atoms occupy four positions at:

[½ 0 0], [0 ½ 0], [0 0 ½], [½ ½ ½]

Gallium atoms occupy four positions at:

[0 0 0], [½ ½ 0], [½ 0 ½], [0 ½ ½]

Figure 3.15 illustrates the crystal structure for the Heusler phase of Ni_2MnGa. Gallium occupies the green sites, manganese occupies the red sites, and nickel occupies the blue sites.

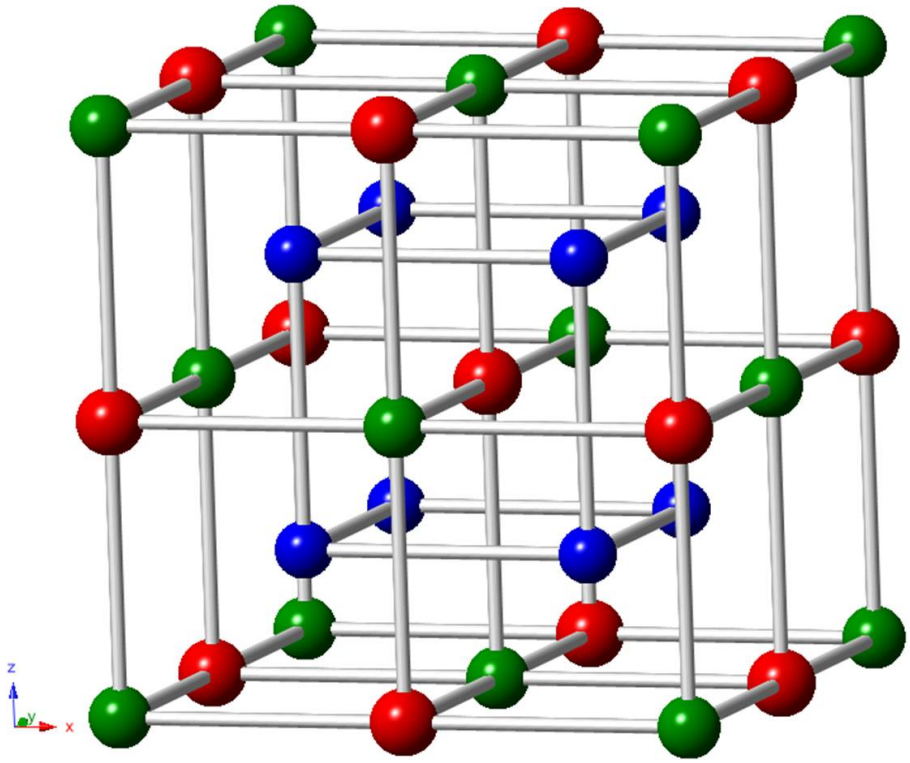

Figure 3.15 Crystal Structure of the Austenite Phase for Ni_2MnGa, Modified from [34]. Gallium Occupies Red Sites, Manganese Green, and Nickel Blue.

3.2.2 Martenisitic Transformations: Phenomenological and Topological Theory

3.2.2.1 Phenomenological Theory

The transformation from the high-symmetry, austenite phase to the lower-symmetry, martensite phase is a diffusionless transformation that occurs by shear distortion of the lattice structure [1]. The phenomenological theory of martensitic transformations [35, 36] uses matrix algebra to describe the total shape change, $\mathbf{P_1}$, which the martensitic transformation imposes to a volume element of austenite. The austenite lattice is transformed to the martensite lattice by

$$\mathbf{P_1 = R P_2 B} \tag{9}$$

In this equation, **B** is the homogeneous distortion, or Bain distortion, $\mathbf{P_2}$ is the lattice invariant shear, and **R** is a rigid-body rotation. The total shape change is decomposed into three transformations, occurring simultaneously. The Bain strain tends to distort all directions and thus there is no invariant plane that could serve as the habit plane. The lattice invariant shear, $\mathbf{P_2}$, serves to deform the martensite phase plastically so that $\mathbf{P_2B}$ produces an undistorted plane. The image of the undistorted plane has to be rotated by **R** in order to become invariant after the complete transformation $\mathbf{RP_2B}$.

There are two options for the deformation $\mathbf{P_2}$, slip or twinning [37]. These mechanisms aid formation of martensite with little or no volumetric change. The formation of an invariant plane by slip and twinning is schematically shown in Figure 3.16.

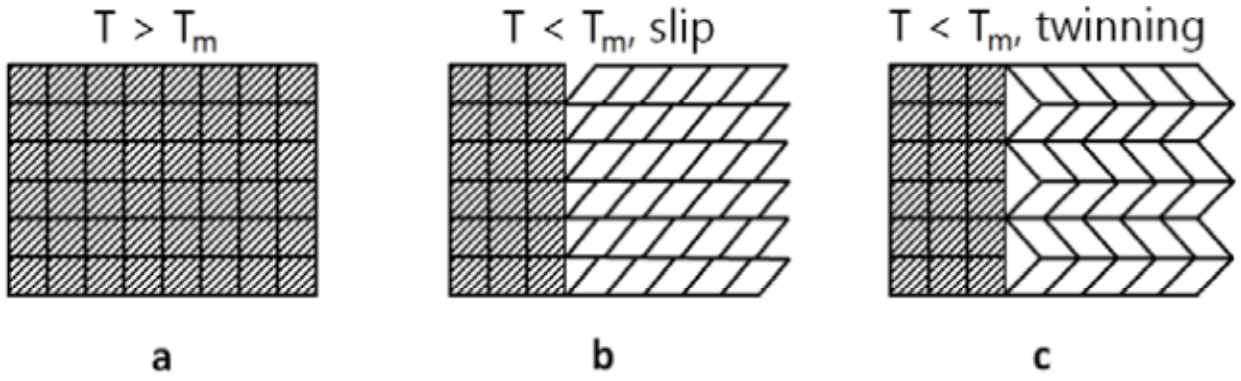

Figure 3.16 Schematic of the Interface of Austenite and Martensite Phases During the Martensite Phase Transformation. (a) Shows the Crystal Structure at a Temperature Greater Than the Martensitic Phase Transformation Temperature. The Crystal Is in the Austenite Phase. (b) and (c) Show the Crystal Structure During the Martensitic Phase Transformation. It Is Necessary for Either Slip (b) or Twinning (c) to Occur to Accommodate the Geometry of the Austenite During Phase Transformation. Reprinted with Kind Permission from [37].

Figure 3.17 is an illustration demonstrating the austenite/martensite interface with its associated invariant plane that separates the austenite from a twinned martensite region.

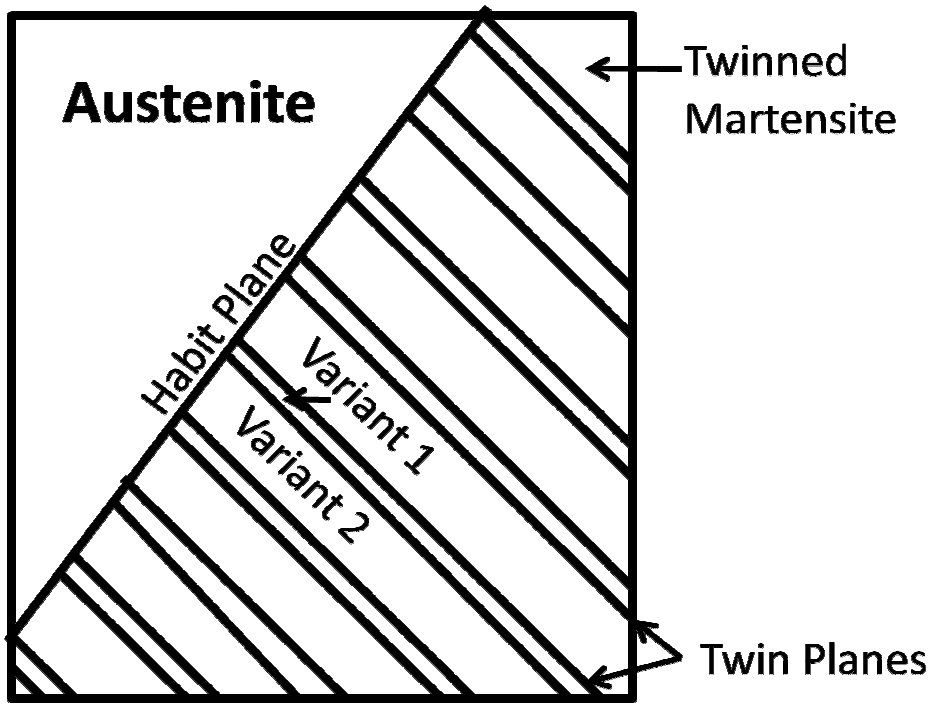

Figure 3.17 Schematic Demonstrating the Austenite/Martensite Interface. The Invariant Plane (Habit Plane) Forms the Interface Between Martensite and Austenite. Twins Form at the Austenite Interface to Accommodate Strain.

During the martensitic transformation in shape-memory materials, the martensite can have different crystallographic orientations with respect to the cubic parent phase. Each unit cell having a different orientation is called a variant. The twins and martensite variants that form arrange themselves in a pattern to minimize the overall strain energy due to the transformation. This behavior is known as “self accommodation” of twinned martensite [1].

The phenomenological theory of martensite transformations predicts the habit plane for many transformations; however, the interface structure and transformation mechanism are not represented. It cannot, for example, explain why habit planes sometimes vary with small changes of composition or mode of formation.

3.2.2.2 Topological Theory

The topological model of martensitic transformations is based on dislocation theory. In this theory, the transformation is modelled in terms of glissile motion of partially coherent interfaces (see Section 3.1.5). The austenite/martensite interface can be modelled as an array of disconnections, superimposed on coherent terraces, and the resulting habit plane orientation and misorientation of adjacent crystals is in close agreement with the predictions of the phenomenological theory [19]. The validity of the disconnection structure of the martensite interface is supported by experimental observations, where high-resolution microscopy has shown step-like character of disconnections in martensite/austenite interfaces [19].

3.2.3 Martensite Structures

Below the martensite phase transformation temperature, several different structures are known to exist in Ni-Mn-Ga alloys, depending on compositions, temperature, and externally applied forces. The most commonly reported structures are the 14-layered structure (14M), the ten-layered structure (10M), and non-modulated (NM or 2M) structure [38].

Composition is the most important factor in determining the martensitic crystal structure at room temperature. Richard et al. [39] characterized the crystal structure of

powdered single crystals with varying composition. Figure 3.18 summarizes their results. In this figure, orthorhombic refers to the 14M structure and tetragonal refers to the 10M structure. Lanksa et al. [40] collected similar data and noted that the non-modulated tetragonal structure was seen in compositions on the upper left of this graph, where Mn concentration is low and Ga concentration is high.

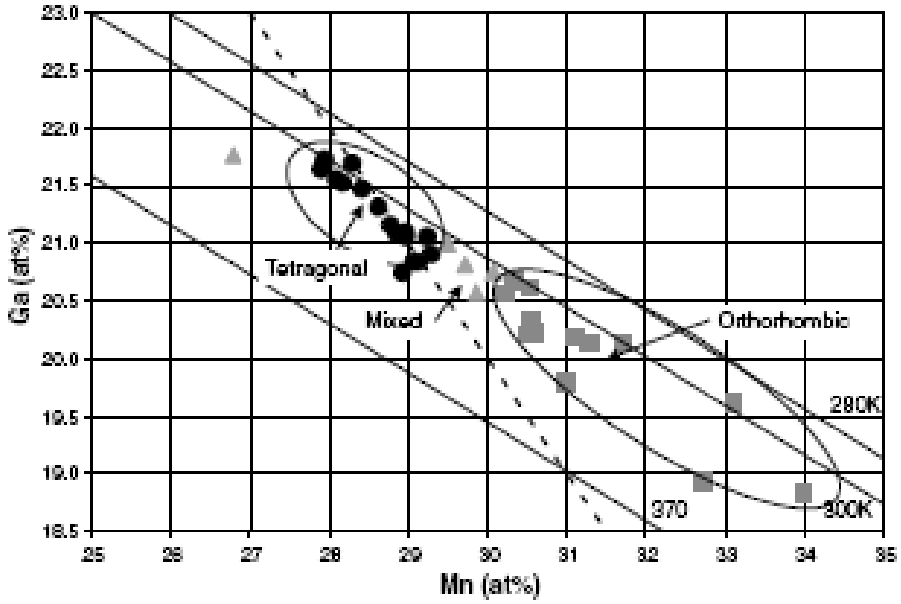

Figure 3.18 Composition Effects on Crystal Structure After Annealing. Orthorhombic Is Plotted with Squares, Tetragonal with Circles, and Mixtures with Triangles. The Solid Sloped Lines Are Different Maretensite Transformation Temperatures. Reprinted with Kind Permission from [39].

Other factors also affect the crystal structure of Ni-Mn-Ga alloys. For example, upon cooling from austenite parent phase, an intermartensitic transformation has been seen [41] in which a modulated martensite formed first and further cooling lead to a non-modulated martensite phase. Upon heating, only a phase transformation from the non-modulated martensite to austenite phase was observed. Transformations upon cooling

from an austenite parent phase to a 10M martensite and further to a 14M martensite have also been observed [42]. Depending on the martensite phase the sample was in when the cooling was stopped, 14M to austenite and 10M to austenite phase transformation have been observed, but no intermartensitic transformations upon heating were seen [42].

Applied stress also impacts the crystal structure. It has been shown that upon cooling and with increasing stress the austenite phase changes to the 10M, then to the 14M, and then to the non-modulated phase or from austenite to the 14M and then to the non-modulated or directly from the austenite to the non-modulated phase [43]. The non-modulated structure is the ground state for martensite [44].

3.2.3.1 Non-Modulated Martensite Structure

The non-modulated lattice results from a tetragonal distortion of the cubic parent phase. There are two separate tetragonal unit cells commonly used to describe the non-modulated structure, both of which have a *c/a* ratio larger than unity. The most commonly reported cell is one that shares an axis system with the parent cubic cell, where the *a* and *b* axes have been compressed and the *c* axis elongated to form a face-centered tetragonal cell [38, 45]. The structure is also sometimes reported as body-centered tetragonal [46]. The relationship between the two axis systems is shown schematically in Figure 3.19. The face-centered unit cell is outlined in black, and the axes are labeled a_1 and c_1. The body-centered tetragonal unit cell is outlined in grey, with axis a_2 and c_2. The *c* axis of the two unit cells are identical, and the relationship between a_1 and a_2 is $a_1 = \sqrt{2}a_2$.

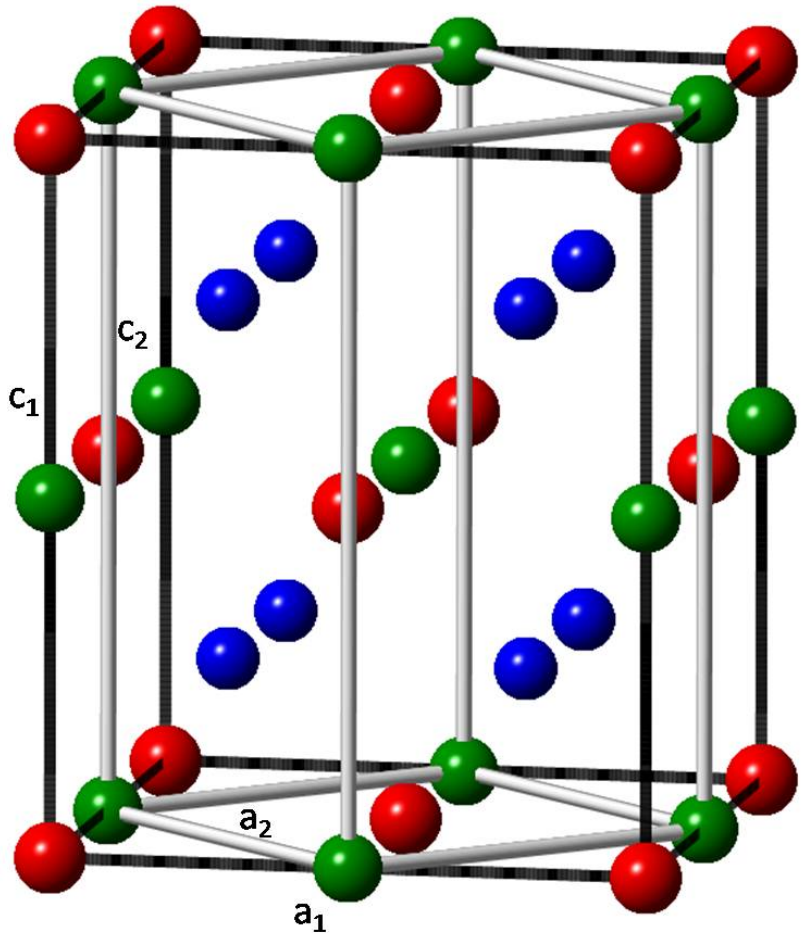

Figure 3.19 Relationship Between the Face-Centered Tetragonal and Body-Centered Tetragonal Unit Cells. The Face-Centered Axis Are Labeled a_1 and c_1. The Body-Centered Tetragonal Axis Are Labeled a_2 and c_2. The c Axis of the Two Coordinate Systems Are of the Same Magnitude, and $a_1 = \sqrt{2}a_2$. Gallium Occupies Red Sites, Manganese Green, and Nickel Blue.

Figure 3.20 shows a high-resolution transmission electron micrograph of a twin boundary between non-modulated variants viewed along the $[010]_T$ zone axis of the face-centered tetragonal structure, and the corresponding diffraction pattern [47]. The arrows indicate the location of the twin boundary. The tetragonal unit cell can be seen in the high-resolution image and is outlined in red.

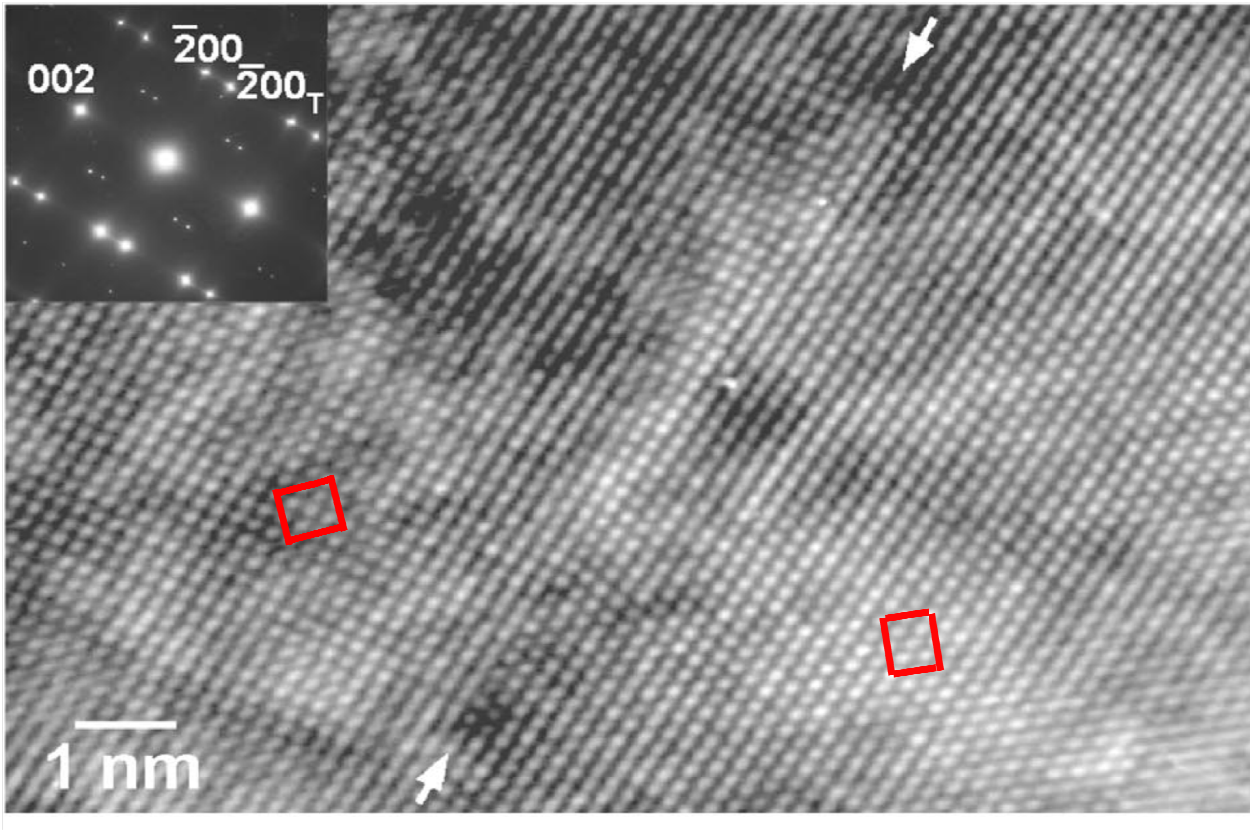

Figure 3.20 High Resolution Transmission Electron Micrograph and Corresponding Electron Diffraction Pattern Viewed Along $[010]_T$, Revealing the Tetragonal Structure of the Non-Modulated Martensite. A Twin Boundary Is Marked by White Arrows. The Tetragonal Unit Cells Are Outlined in Both Twin Variants in Red. Reprinted with Kind Permission from [47].

Typical lattice parameters for the non-modulated cell are given in Table 3.1 for both axis systems [45].

Table 3.1 Lattice Parameters of the Non-Modulated Martensite Structure Reported for Both the Face-Centered Tetragonal Unit Cell and the Body-Centered Tetragonal Unit Cell.

	Lattice Parameters [Å]		
Unit cell	*a*	*b*	*c*
Face-Centered Tetragonal	5.46	5.46	6.58
Body-Centered Tetragonal	3.86	3.86	6.58

3.2.3.2 Modulated Structures

The superlattice diffraction peaks due to the modulation of the 14M and 10M unit cells are of very low intensity and are often not seen in X-ray diffraction experiments; therefore, the modulated cells are often described by unit cells that are deduced from the fundamental diffraction spots and do not include the modulation [38]. Both the modulated unit cell and the unit cell deduced from fundamental diffraction spots will be discussed for the modulated structures.

The modulated martensites differ in the arrangment of $(101)_c$ planes of the cubic austenitic parent phase. These planes undergo a systematic displacement resulting in a long-periodic structure. The axis $[010]_C$ and $[010]_M$, where M signifies monoclinic, are identical. Following the Zdanov notation [48], the stacking sequence is described by a symbol $(\overline{XY})_m$ where *X* and *Y* are the numbers of successive displacements in the $[\bar{1}00]_M$ and $[100]_M$ directions and m is the number of repetitions of $(\overline{XY})$ units that complete a martensite unit cell. Otsuka et al. [49] suggested the use of the number *mn* followed by a capital letter indicating the crystal axis system, where *n=X+Y*, to describe the martensite

as "*mn* layered." The layered structures are therefore called 14M and 10M and denoted $(\bar{5}2)_2$ and $(\bar{3}2)_2$, respectively.

14M Martensite Structure. The fundamental diffraction spots in the 14M structure describe an orthorhombic crystal structure with a *c*/*a* ratio of around 0.90 [45]. TEM diffraction patterns show six extra spots between the fundamental diffraction spots. The unit cell accounting for the extra diffraction spots is a stacked body-centered monoclinic cell (space group *I2/m*), shown in Figure 3.21 along the $[010]_{14M}$ direction. The $(\bar{5}2)_2$ stacking sequence is emphasized with dashed lines. Gallium occupies the red sites, manganese occupies the green sites, and nickel occupies the blue sites.

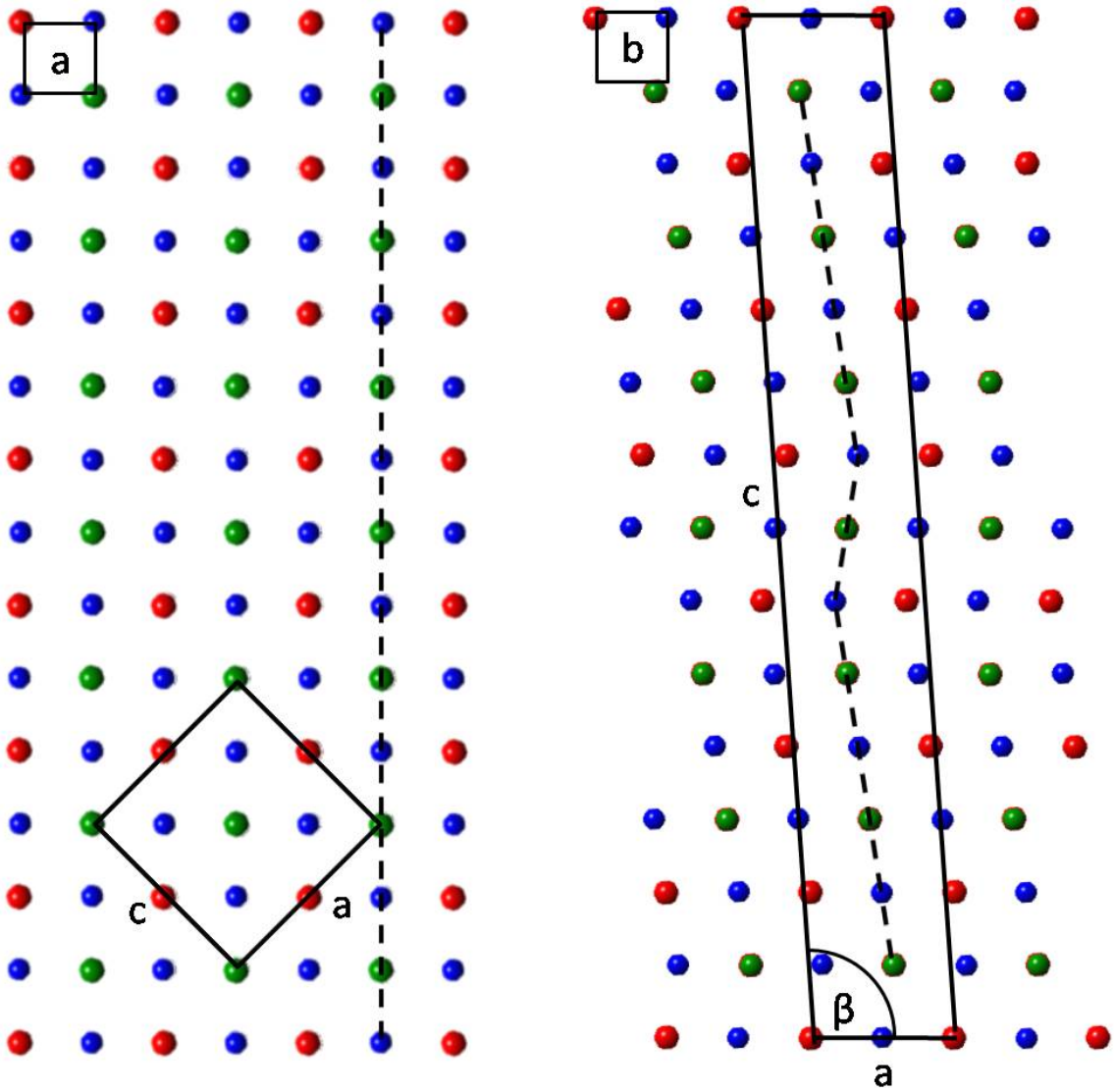

Figure 3.21 Structure of the (a) Cubic Austenite Phase and (b) 14M Structure Represented as a Body-Centered Monoclinic Unit Cell (Space Group *I2/M)* Viewed Along $[010]_{14M}$. The $(\bar{5}2)_2$ Stacking Sequence Is Emphasized with Dashed Lines. Gallium Occupies Red Sites, Manganese Green, and Nickel Blue.

Figure 3.22 is an X-ray diffraction pattern of the 14M structure, modified from [38]. The pattern is indexed in accordance with the stacked monoclinic cell, index M, and

according to the orthorhombic cell, index O. All of the high-intensity peaks can be indexed in either reference frame.

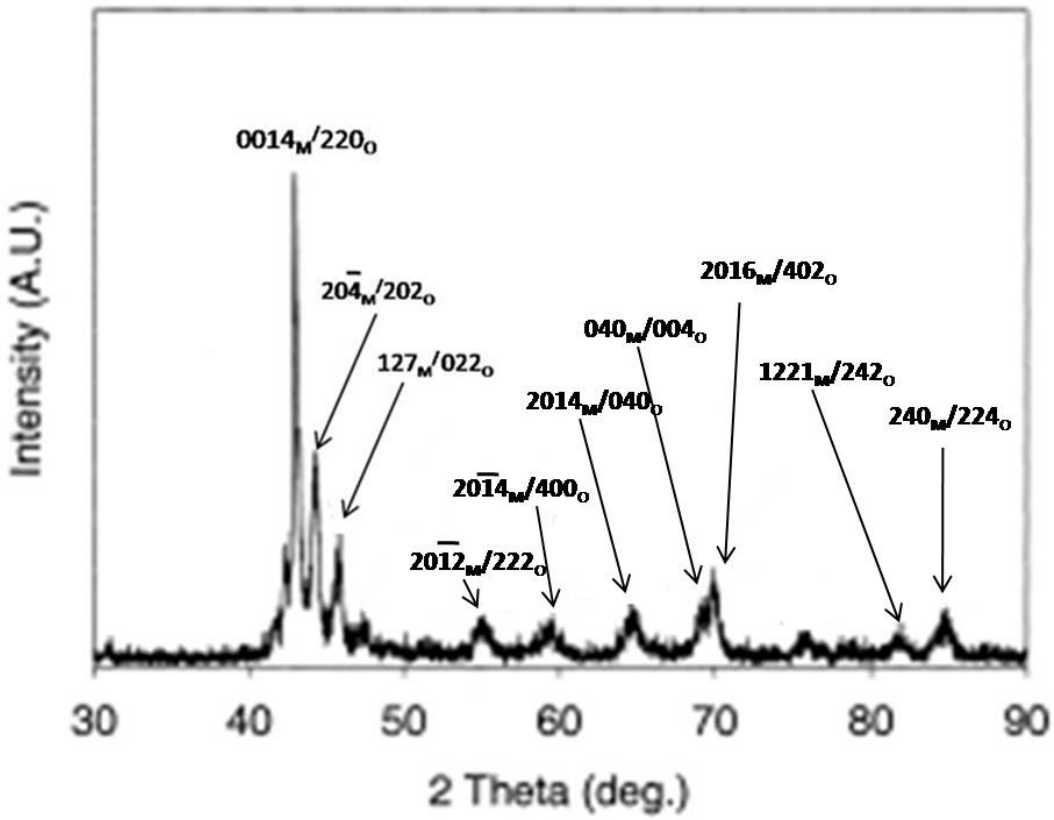

Figure 3.22 X-Ray Diffraction Pattern of the 14M Martensite Structure. All of the High-Intensity Peaks Can Be Indexed According to the Stacked Monoclinic Cell (M) or the Orthorhombic Cell (O). Reprinted with Kind Permission from [38].

Figure 3.23 (a) is a TEM diffraction pattern of the 14M structure [38]. The diffraction pattern shows the six extra spots in between the fundamental reflections and is indexed according to the monoclinic structure. The reflection 107 is a result of chemical ordering. Figure 3.23 (b) is a high-resolution micrograph [47] of the 14M structure. The high-resolution micrograph was not taken in the same location as the diffraction pattern;

however, the micrograph emphasizes the $(\bar{5}2)_2$ stacking sequence seen in the 14M structure.

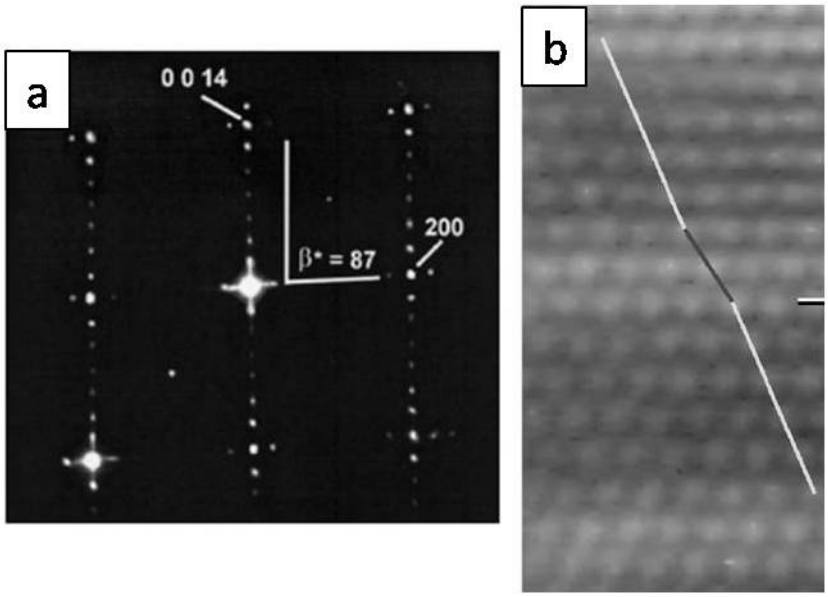

Figure 3.23 (a) Experimental Electron Diffraction Pattern of the 14M Structure, Which Reveals the 7 Extra Spots Between the Primary Diffraction Spots. The Diffraction Pattern Is Indexed According to the Monoclinc Cell. Reprinted with Kind Permission from [38]. (b) High-Resolution Transmission Electron Micrograph of the 14M structure, the Lines Drawn on the Image Emphasized the $(\bar{5}2)_2$ Stacking Sequence. Reprinted with Kind Permission from [47].

Table 3.2 gives typical lattice parameters found for the 14M structure given in terms of the monoclinic axis system [38] and the orthorhombic axis system [45].

Table 3.2 Lattice Parameters for the 14M Martensite Structure Given for Both the Monoclinic and Orthorhombic Unit Cells.

	Lattice Parameters [Å]			Angles		
Unit cell	*a*	*b*	*c*	*α*	*β*	*γ*
Monoclinic	4.23	5.5	29.	90	93.5	90
Orthorhombic	6.19	5.8	5.53	90	90	90

10M Martensite Structure. Fundamental diffraction spots of the 10M structure show a tetragonal unit cell with a *c*/*a* of about 0.94. TEM diffraction patterns show four extra spots between the fundamental reflections. There is currently debate about the nature of the stacking of atomic planes in the 10M unit cell. It is possible that the 10M cell is built by long period stacking of planes, in the form $(\bar{3}2)_2$. Alternatively, a periodic shuffling of the basal planes may occur, the displacement of each plane from its original position being given by a function containing harmonic terms [38]. An example unit cell built using atomic positions derived using the latter approach [50] is given in Figure 3.24 in the $[010]_{10M}$ direction. This is a body-centered monoclinic cell (space group *I2/m*). Gallium occupies the red sites, manganese occupies the green sites, and nickel occupies the blue sites.

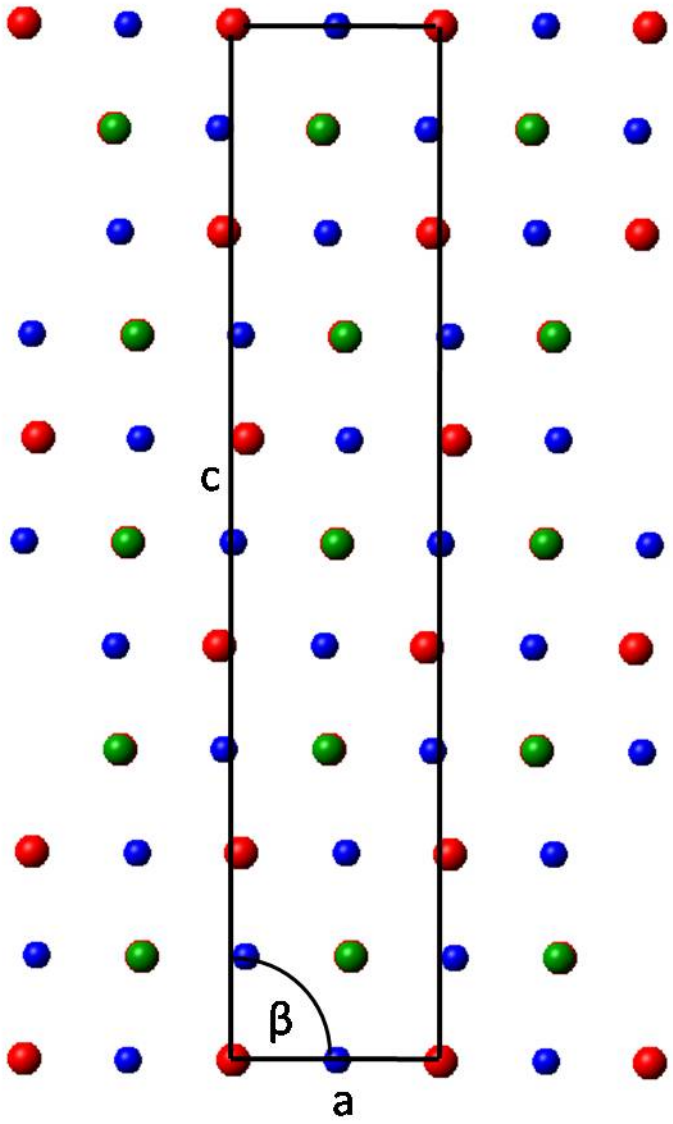

Figure 3.24 10M Martensite Structure Represented as a Body-Centered Monoclinic Cell (space group *I2/m*) Viewed Along the $[010]_{10M}$ Direction. Gallium Occupies the Red Sites, Manganese Occupies the Green Sites, and Nickel Occupies the Blue Sites.

Figure 3.25 (a) [38] shows a selected area diffraction pattern from a 10M structure, indexed according to the monoclinic unit cell. The SADP shows the four extra spots between the fundamental diffraction spots. A high-resolution image of the 10M

sample is also shown below in Figure 3.25 (b) [47] (not from the same area as the diffraction pattern), which shows the stacking sequence.

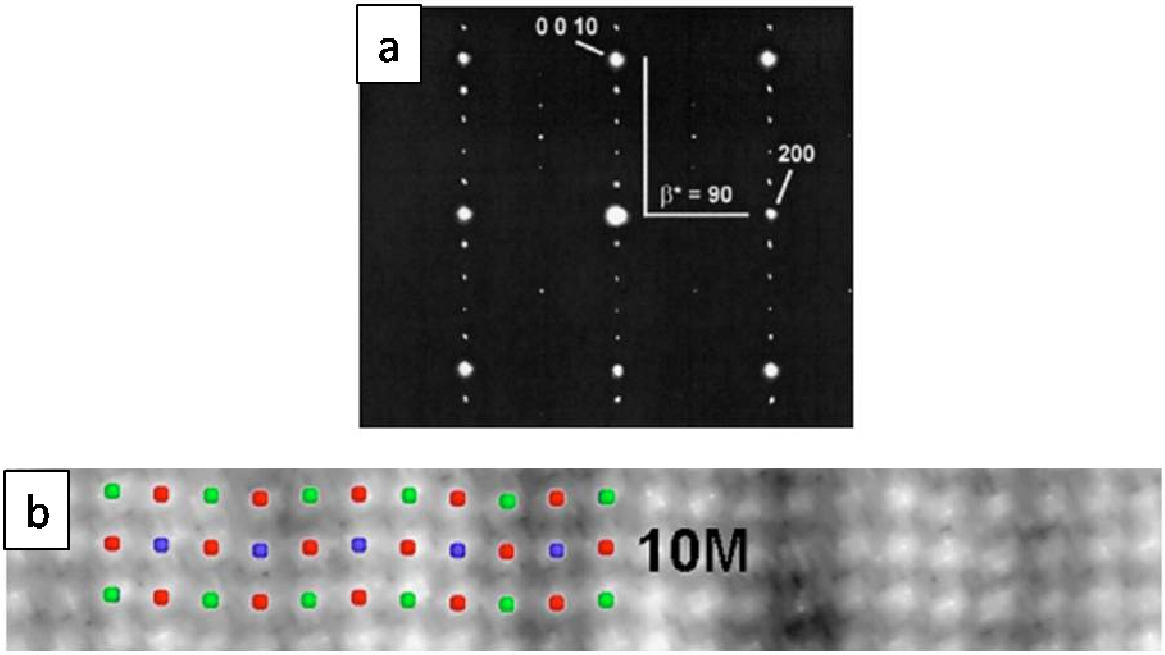

Figure 3.25 (a) Selected Area Diffraction Pattern of the 10M Structure Reveals Four Spots in Between the Primary Diffracted Spots. The Pattern Is Indexed According to the Monoclinic Cell. Reprinted with Kind Permission from [38]. (b) High Resolution Transmission Electron Mircrograph Showing the Atomic Positions in the 10M Structure. Reprinted with Kind Permission from [47].

Table 3.3 gives typical lattice parameters for the 10M structure in terms of the monoclinic [38] and tetragonal [45] unit cells.

Table 0.3 10M Lattice Parameters Presented for Both the Monoclinic and Tetragonal Unit Cells. Lattice Parameters from [38] and [45].

	Lattice Parameters [Å]			Angles		
Unit cell	*a*	*b*	*c*	*α*	*β*	*γ*
Monoclinic	4.24	5.66	20.5	90	90.5	90
Tetragonal	5.94	5.94	5.59	90	90	90

3.3 Magnetoplasticity

A macroscopic change of shape occurs in Ni-Mn-Ga when exposed to a magnetic field. Upon the removal of the magnetic field, the alloy does not return to its original shape; however, the original shape can be achieved by rotating the magnetic field. This effect is known as magnetoplasticity [1]. Significant magnetoplasticity occurs in single crystals. Magnetoplasticity is suppressed in bulk polycrystals.

The magnetoplasticity of MSMAs takes place through the motion of twin boundaries. Upon the application of a magnetic field, the magnetic moment of the twins tends to align with the magnetic field in order to reduce the Zeeman energy. Because Ni-Mn-Ga exhibits magnetic anisotropy, the rotation of the magnetic moments increases the magneto crystalline energy in twin variants that do not have their easy axis of magnetization parallel with the applied magnetic field. This effect drives twin rearrangement [37]. When one twin variant realigns, the boundary between a set of twins moves. Figure 3.26 illustrates this concept. The initial state shows two twin variants, labeled 1 and 2. They are separated by the twin boundary. Upon the application of the magnetic field, the magnetic moments will tend to align with the applied field, causing variant realignment and twin-boundary motion.

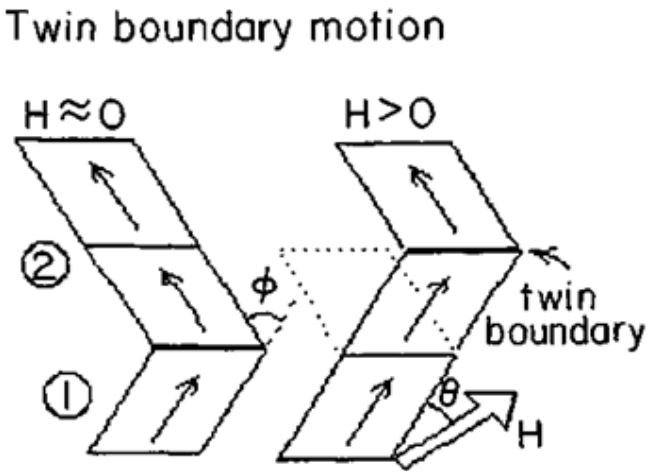

Figure 3.26 Schematic of Twin Boundary Motion. (a) The Initial Twin Structure Contains Two Twin Variants, 1and 2. The Top Variant's Magnetic Moment Is Oriented to the Left While the Bottom Variant's Magnetic Moment Is Oriented to the Right. Upon the Application of a Magnetic Field, (b) the Magnetic Moment in the Top Variant Aligns with the Field. The Twin Boundary Moves Up and the Bottom Variant Grows at the Expense of the Top Variant. Reprinted with Kind Permission from [37].

To reach the maximum shape change, the MSMA needs to be completely in one twin variant or the other, so that all *c* directions are aligned. The maximum theoretic magnetic-field-induced strain is equal to the spontaneous strain $\varepsilon = 1 - c/a$. The *c/a* ratio depends on the crystal structure of the martensite phase. Table 3.4 gives the theoretical maximum strain for each martensite crystal structure based on lattice parameters given in Section 3.2, along with the maximum MFIS found experimentally. Strains close to the theoretical maxima have been achieved for the modulated structures [7, 8, 45]; however, the non-modulated structure has high twinning stresses and only very small MFIS has been achieved [51].

Table 3.4 Maximum Theoretical MFIS for Each of the Martensite Structures and the Maximum MFIS Seen Experimentally. The 14M and 10M Structures Have Achieved MFIS Close to the Theoretical Max; However, the NM Structure Has High Twinning Stresses and Only Very Small MFIS Has Been Seen Experimentally.

Structure	Theoretical Strain %	Max Experimental MFIS %
14M	10.66	9.6 [8]
10M	5.89	5.8 [45]
NM	20.5	0.17 [51]

On the microscopic scale, twins grow and shrink by the movement of dislocations located in steps on the twin boundary [19]. A defect with both step and dislocation character is termed a disconnection [18, 19] and is discussed in detail in Section 3.1.5. Moving the disconnection requires a force, which can be induced by a magnetic field or a mechanical stress. An applied magnetic field causes a magnetic force, F_M, on the disconnections. The maximum force, F_M, that can be produced by a magnetic field that is larger than the saturation field on a twinning disconnection is [52]:

$$F_M = hK \tag{10}$$

where K is the magnetic anisotropy constant and h the step height of the disconnection. The magneto-stress, τ_M, on the twinning plane in the twinning direction is a shear stress. With s being the twinning shear $s = b_t/h$, the maximum magnetostress is:

$$\tau_M = K / s \tag{11}$$

The magnetic field exerts a magnetic force on the disconnection and causes the disconnection to move. The motion of the disconnections causes motion of the twin boundary and the growth of one twin and shrinkage of the other.

CHAPTER 4: EXPERIMENTAL

The twinned microstructure and the disconnection structure of individual twins were characterized in Ni-Mn-Ga with non-modulated martensite samples. The non-modulated structure was chosen because of its simplicity in comparison to the other martensite structures, with the intention to later apply the knowledge gained to the more complicated structures. The microstructure of the non-modulated structure is, itself, important to understand. The non-modulated structure is frequently encountered as the ground state for martensite [44].

4.1 Sample Preparation

The dislocation structures and branching of twins in non-modulated Ni-Mn-Ga were studied in polycrystalline samples. Polycrystalline Ni-Mn-Ga of nominal composition $Ni_{46.75}Mn_{34}Ga_{19.25}$ (at%) was prepared in a Reitel induction furnace from the constitutive metals Ni 99.9% (Alfa Aesar), Mn 99.9% (Alfa Aesar), and Ga 99.999% (Sigma Aldrich) and cast into a copper mould. During the casting, 2.5% of the mass of the ingot was lost. This is presumed to be primarily Manganese loss.

The bulk ingot was sectioned and mechanically polished down to 1 micron grit size for XRD experiments. A section was then mechanically thinned to a foil thickness (80-120 μm) and 3 mm disks were punched using a Model 656 Disc Punch (Gatan, Inc). Thin foils were double jet electro-polished in a solution of 700 mL methanol (Aldrich,

USA) and 300 mL 69.9% (vol.) nitric acid (Aldrich, Aldrich) in a TenuPol 3 (Struers) system at 243 K and 10 V.

4.2 Transmission Electron Microscopy

Transmission electron microscopy is a microscopy technique in which an electron beam is transmitted through an ultra thin specimen, interacting with the specimen as it passes through. An image is formed by the electrons that pass through the specimen. The image is magnified and focused onto an imaging device or detected by a sensor such as a CCD camera.

A transmission electron microscope (TEM) is composed of several main components, including a vacuum system in which the electrons travel, an electron emission source for generation of the electron stream, and a series of electromagnetic lenses and apertures [53]. The lenses and apertures are used to guide and manipulate the beam. A device to allow the insertion into, motion within, and removal of specimens from the beam path is also required. Imaging devices are subsequently used to create an image from the electrons that exit the system.

There are several different types of electron sources. The most common consists of a thermionic gun capable of accelerating the electrons through a selected potential difference in the range of 40-200 kV [54]. A field emission gun can also be used in which a single crystal of tungsten is subjected to an extremely high electric field to create the beam of electrons [54]. The condenser lens assembly demagnifies the beam emitted by the gun and controls its diameter as it hits the specimen. This allows control of the area of illumination and the intensity of the beam. An aperture is present between the condenser lenses (condenser aperture), which can be used to control the convergence angle. The

first condenser lens is often labeled ‘spot size’ and sets the demagnification of the gun crossover. The second lens, called ‘intensity’, provides control of the convergence angle of the beam leaving the condenser assembly. As the convergence angle is increased, the beam diameter at the specimen decreases until it reaches its minimum, when the beam is focused on the sample. The specimen is held between pole pieces of the objective lens.

Figure 4.1 shows a ray diagram of the electrons through the TEM. The objective lens forms the first intermediate image and diffraction pattern, one or the other of which is enlarged by subsequent projector lenses and displayed on the viewing screen. A diffraction pattern is always formed in the back focal plane of the objective lens. The intermediate lens can be switched between two settings. In the image mode, Figure 4.1(a), the intermediate lens is focused on the image plane of the objective lense. In diffraction mode, Figure 4.1(b), the intermediate lens is focused on the back focal plane of the objective lens and the diffraction pattern is projected onto the viewing screen. There are several sizes of objective aperture, which can be inserted into the column in the back focal plane. This aperture can control the contrast that is seen in the image.

For all TEM results presented in this thesis, the foils were imaged at 200kV in a JEOL 2100 HR (JEOL LTD) TEM operated with a LaB_6 filament.

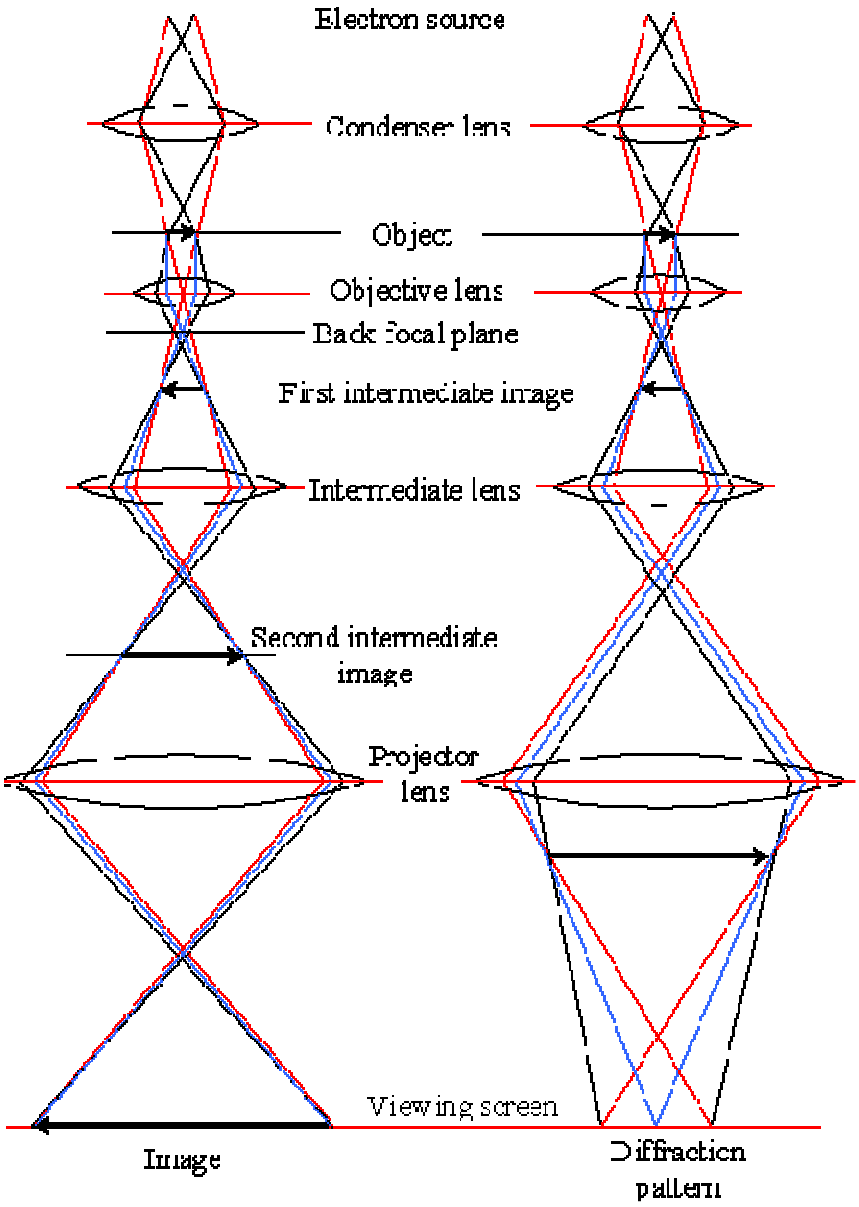

Figure 4.1 Ray Diagram Showing the Electron Path in a TEM for a) Formation of an Image, and b) Formation of a Diffraction Pattern.

The objective aperature can be used to allow either the undeflected beam or a diffracted beam to form the image, giving strong contrast from regions that are diffracting strongly. Strong diffraction contrast occurs when the crystal is oriented such that only the undeflected beam and one low index diffracted beam are present in the diffraction

pattern. This is known as a two-beam condition. The sample is tilted so that a Kikuchi line runs through the undeflected beam, and the parallel kikuchi line runs through a strongly diffracted beam. In bright-field imaging, the objective aperture is used to stop all diffracted beams and only permits undeflected electrons to contribute to the image, as seen in Figure 4.2(a). If the aperture is displaced, it can be used to select a particular diffracted beam, as shown in Figure 4.2(b). This is known as displaced-aperture, dark-field imaging. If the dark-field image is created by displacing the aperture in this way, aberrations are likely to be introduced since all the imaging electrons are traveling far from the optical axis, where spherical aberrations are large.

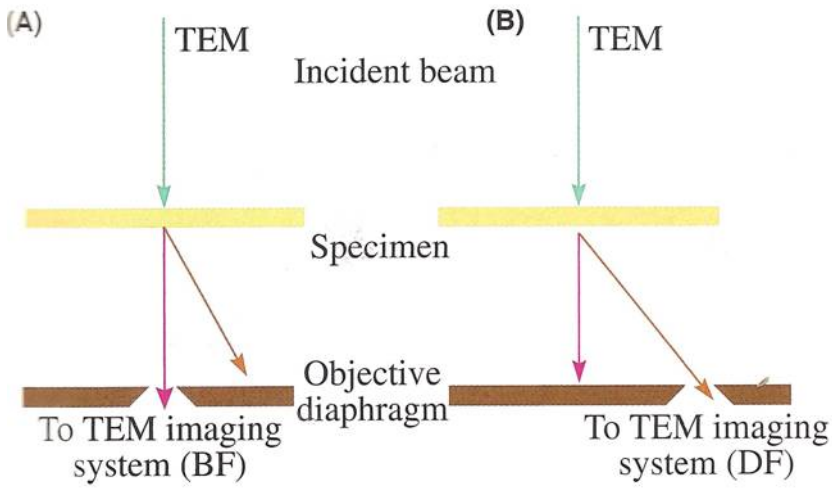

Figure 4.2 Schematic Illustrating the Use of an Objective Aperture in the TEM to Select (A) the Direct or B) the Scattered Electrons Forming BF and DF Images, Respectively. Reprinted with Kind Permission from [53].

A better method is to tilt the incident electron beam so that the chosen diffracted beam travels along the optical axis and passes through the centered aperture. This method is shown schematically in Figure 4.3.

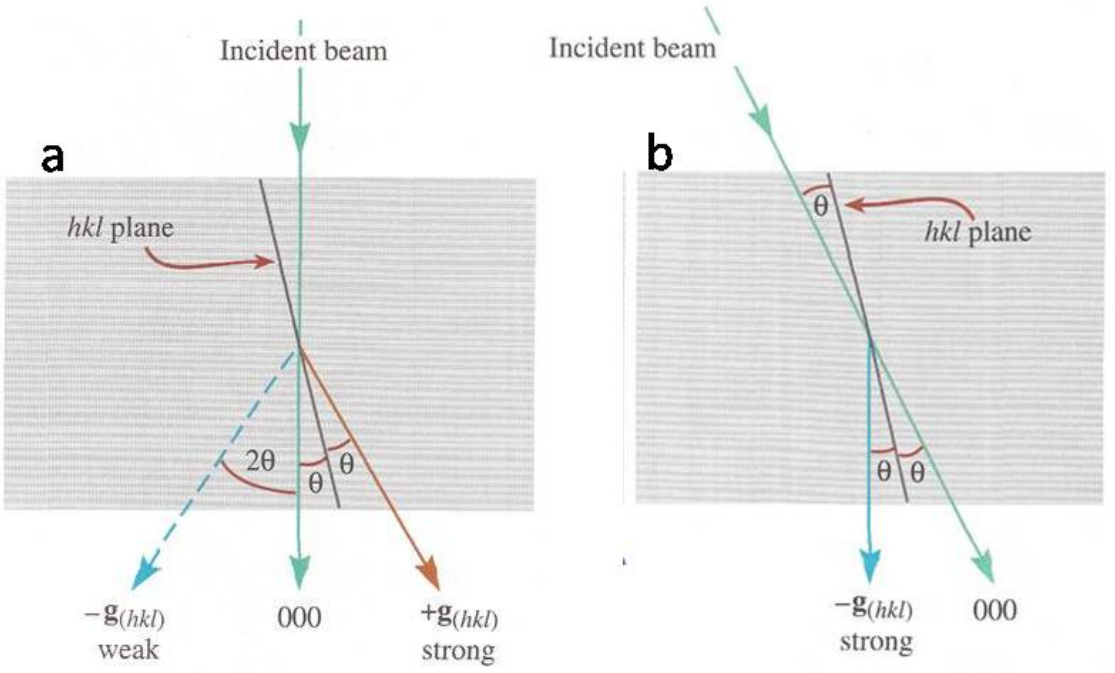

Figure 4.3 a) The Standard Two-Beam Condition with Only the 000 and hkl Spots Bright. B) The Incident Beam Is Tilted through 2θ So That the Excited g_{hkl} Spot Moves onto the Optic Axis. Reprinted with Kind Permission from [53].

Analysis of TEM micrographs is not directly straightforward and requires significant knowledge of electron diffraction and contrast mechanisms. The following section provides the basic theoretical background of diffraction and contrast mechanisms in the TEM.

4.2.1 Electron Diffraction

When the electron beam interacts with a perfect crystal, some of the constituent atoms will cause elastic scattering of the beam. The incident electron beam is locally coherent, and any scattered waves that are also in phase with one another will reinforce and lead to a strong beam of electrons, whereas any scattered waves that are out of phase

will not reinforce. In Figure 4.4, the A and B atoms scatter the incident wave. The scattered waves at D will be in phase if the path length of the electrons scattered from atom A and the electrons scattered from atom B differ by an integral number of the wavelength.

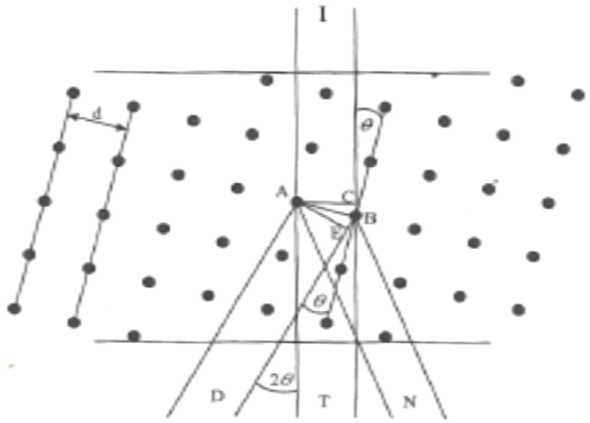

Figure 4.4 Scattering of an Incident Beam of Electrons (I) by a Crystalline Specimen. The Beam May Emerge from the Other Side of the Specimen Undeviated (T), or Having Been Diffracted (D) Form Atomic Planes of Spacing *d*. In Other Diffracted Directions (N), the Waves Did Not Reinforce and No Diffracted Spot Forms. Reprinted with Kind Permission from [54].

The condition for reinforcement is known as Bragg's law, and is given as

$$2d \sin\theta = n\lambda \tag{12}$$

where d is the spacing between the planes of atoms that are scattering the electrons, or interplanar spacing, and λ is the wavelength of the incident beam. The integer n is the order of diffraction; however, in electron diffraction it is conventional to consider only the first order of diffraction, $n = 1$. Higher orders can be described as first-order by modifying the *hkl* such that, for example, second-order diffraction (n=2) from 100 is equivalent to first-order diffraction (n=1) from 200.

Because the wavelength of electrons is much smaller than the spacing of lattice planes, the Bragg angles for electron diffraction are very small. Therefore, there will be strong diffraction only from lattice planes that are almost parallel to the electron beam.

Each type of plane in a crystal will have a different spacing and a different density of atoms per unit area, resulting in different intensities of electron diffraction for each type of plane. The theory of kinematical electron diffraction can be used to predict the planes in crystals that give zero diffracted intensity. The intensity of a diffracted beam is proportional to the structure factor squared, which is given by:

$$F_{hkl} = \sum_{j=1}^{r} f_j(\theta) \exp[-2\pi i(hu_j + kv_j + lw_j)] \tag{13}$$

The structure factor is obtained by adding up the contribution to electron scattering made by each atom in the unit cell, taking into account the phase of each wave that is scattered. Since the crystal is periodic, this only has to be done for one unit cell of the crystal, not a complete specimen. In Equation 13, u_j v_j w_j give the coordinates of the j^{th} atom. The factor $f_j(\theta)$ is the scattering factor, or atomic form factor, of the j^{th} atom, and the exponential factor keeps track of the phase of each scattered wavelet. In the kinematic approximation, which disregards effects of multiple scattering events, the structure factor can be used to predict which lattice planes result in constructive interference, and with what intensity.

4.2.2 Contrast Mechanisms

There are three basic contrast mechanisms: mass-thickness contrast, diffraction contrast, and phase contrast. All three may contribute strongly to the appearance of the TEM image.

4.2.2.1 Mass Contrast

In a thin specimen, the majority of electrons that enter the top of a sample will exit through the bottom; however, many will have been scattered. The effect of an aperture in the back focal plane of the objective lens is to stop all electrons that have been scattered through an angle greater than the angle selected for by the aperture. Regions of a specimen that are thicker, or have a higher density, will scatter more strongly. This results in more electrons being deflected through an angle larger than the aperture selects for. These areas will appear darker in the image.

4.2.2.2 Diffraction Contrast

Any defect that changes the orientation and spacing of the diffracting planes will typically cause diffraction contrast. Such defects include dislocations, stacking faults, and other crystallographic defects. For most real samples, the electron is likely to be diffracted numerous times, and the dynamical theory must be used for a quantitative analysis. The two-beam approximation is used when discussing dynamical theory. The Howie-Whelan equations [55] describe the amplitudes of the undeflected (subscript 0) and diffracted (subscript g) waves as a function of z, the distance through a perfect crystal.

$$\frac{d\phi_0}{dz} = \frac{i\pi}{\xi_0}\phi_0 + \frac{i\pi}{\xi_g}\phi_g \exp[2\pi i s z] \tag{14}$$

$$\frac{d\phi_g}{dz} = \frac{i\pi}{\xi_g}\phi_0 \exp[-2\pi i s z] + \frac{i\pi}{\xi_0}\phi_g \tag{15}$$

The first term in each equation arises from scattering from the undeflected beam and the second term arises from scattering from the diffracted beam. The equations show

that the amplitude of each wave changes as the wave progresses through the crystal due to contribution from the other. The variable *s* is the vector describing the deviation of the Ewald sphere from reciprocal lattice point, known as the deviation parameter. ξ is a constant of the material for a particular value of *g*, and is known as the extinction distance. It is given by

$$\xi_g = \frac{\pi V_c \cos\theta_B}{\lambda F_g} \tag{16}$$

where V_c is the volume of the unit cell, λ is the electron wavelength, θ_B is the Bragg angle, and F_g is the structure factor.

The Howie-Whelan equations can be solved analytically for a perfect crystal. When integrating over the whole crystal thickness, the intensity at the surface of the direct and diffracted beams can be calculated. The diffracted beam (dark field) intensity for a perfect crystal of thickness *t* is

$$I_g = \frac{\sin^2(\pi t s')}{(\xi_g s')^2} \tag{17}$$

The variable *s*' is known as the effective deviation parameter, given by

$$s' = [s^2 + \left(\frac{1}{\xi_g}\right)^2]^{1/2} \tag{18}$$

A crystal defect that disturbs the planes will locally modify the deviation parameter. When a defect is present, the Howie-Whelan equations can be re-written as:

$$\frac{d\phi_0}{dz} = \frac{i\pi}{\xi_0}\phi_0 + \frac{i\pi}{\xi_g}\phi_g \exp[2\pi i(sz + \mathbf{g}\cdot\mathbf{R}] \tag{19}$$

$$\frac{d\phi_g}{dz} = \frac{i\pi}{\xi_g}\phi_0 \exp[-2\pi i(sz + \mathbf{g}\cdot\mathbf{R}] + \frac{i\pi}{\xi_0}\phi_g \tag{20}$$

In these equations, **g** is the reciprocal lattice vector that describes the planes that are diffracting, and **R** is the displacement of atoms from their lattice positions due to the defect. These equations are just as before, with the addition of the $2\pi i\mathbf{g}\cdot\mathbf{R}$ factor. This additional phase is termed α,

$$\alpha = 2\pi i\mathbf{g}\cdot\mathbf{R} \tag{21}$$

The factor **g**·**R** is a measure of the modulation of the electron wave as it travels through the defect. When **g**·**R** is zero or an integer, the displacements do not disturb the operating planes and so the defect is invisible.

Two specific types of defects, stacking faults and dislocations, occur frequently in shape-memory material. The contrast caused by each is now discussed in detail.

Stacking Faults. Stacking faults are planar defects. The displacement of atoms, **R**, is effectively zero for all positions above the fault plane and has a non-zero but constant value everywhere below the fault. Since **R** is constant, α is also constant.

The Howie-Whelan equations can be solved for the case of a constant α. The intensity of the diffracted beam is found to be [53]

$$I_g \propto \frac{1}{s^2}[A - B\cos(2\pi st')] \tag{22}$$

where t' is the distance of the fault below the center of the slice ($t'=t_1-t/2$ where t_1 lies between 0 and t and $t/2$ is the center of the foil); therefore, the contrast depends on

both the thickness of the sample and depth of the fault. The intensity will generally vary periodically, unless the beam is perpendicular to the stacking fault. The characteristic contrast of stacking faults consists of fringes running parallel to the intersection of the fault with the specimen surface [53]. A typical example of fault contrast is shown in Figure 4.5.

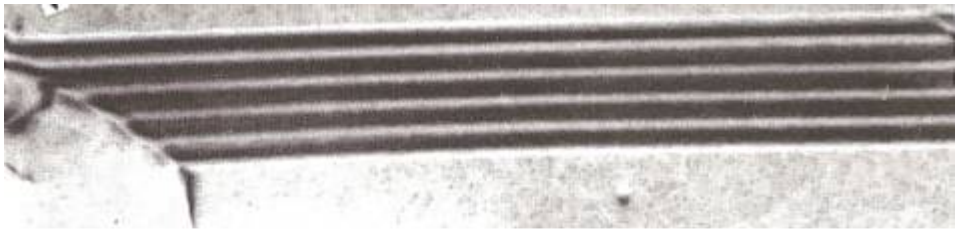

Figure 4.5 Characteristic Contrast of Stacking Faults. Fringes of Alternating High and Low Contrast Run Parallel to the Intersection of the Fault with the Specimen Surface. Reprinted with Kind Permission from [53].

Dislocations. Near the core of a dislocation, lattice planes are usually bent quite severely, but the extent of lattice bending decreases at greater distances. If the crystal away from the dislocation is set close to a two-beam condition (i.e., near to but not exactly at Bragg angle), then the bent planes on one side of the dislocation core may reach the Bragg orientation, and will diffract more strongly than their surroundings [53]. This is demonstrated schematically in Figure 4.6.

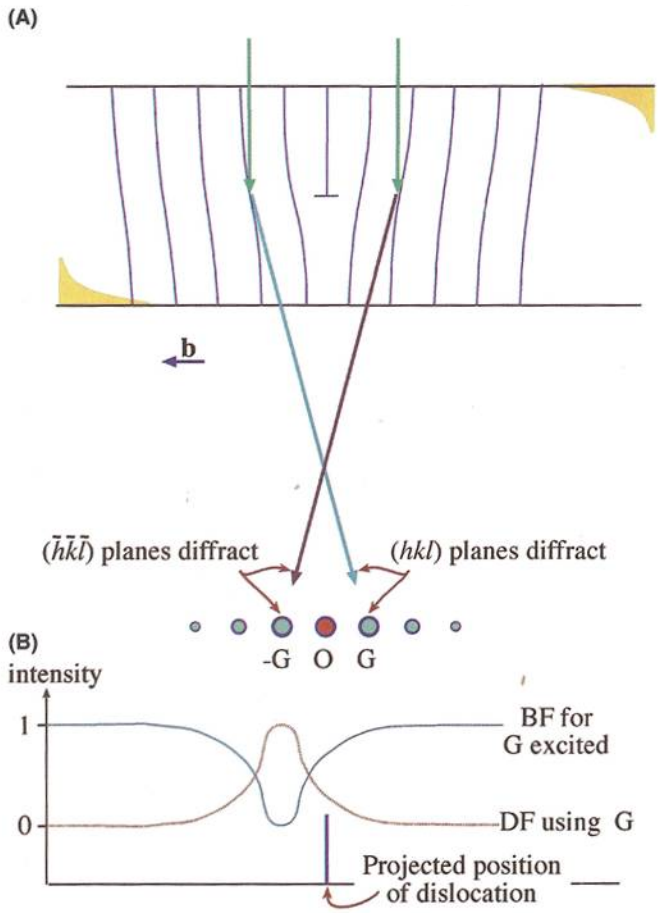

Figure 4.6 Illustration of Contrast Created by Dislocations. (A) The Specimen Is Tilted Slightly Away from the Bragg Condition. The Distorted Planes Close to the Edge Dislocation Are Bent Back into the Bragg-Diffracting Condition. (B) Schematic Profiles Across the Dislocation Image Showing That the Defect Contrast Is Displaced from the Projected Position of the Defect. Reprinted with Kind Permission from [53].

The dislocation will therefore appear as a dark line in a bright-field image. A general rule is that dislocations are invisible if $\mathbf{g}\cdot\mathbf{b} = 0$. This is true for screw dislocations; however, for edge and mixed dislocations, $\mathbf{g}\cdot\mathbf{b}\times\mathbf{u} = 0$ must also be true, where **u** is the line sense [53]. Partial dislocations have non-integral values of $\mathbf{g}\cdot\mathbf{b}$. The rule of thumb for visibility is that a partial dislocation is visible if $\mathbf{g}\cdot\mathbf{b} > 1/3$ [53].

4.2.2.3 Phase Contrast

Phase contrast results whenever electrons of different phases are allowed to pass through the objective aperture. Since most electron scattering mechanisms involve a phase change, this means that some sort of phase contrast is present in every image. Phase contrast is most useful in obtaining high-resolution electron micrographs.

4.3 X-Ray Diffraction

The crystal structure of the bulk polycrystalline sample was analyzed via X-ray diffraction (XRD) using a Bruker D8 Discover diffractometer with a Cu Kα source equipped with a Göbel mirror, a monochromator and point detector. NIST corundum standards were used to characterize the peak positions and widths. If the peak position was within 0.04° in 2θ of the reference, the detector position was deemed acceptable according to ASTM standards.

For polycrystalline samples with many randomly orientated crystallites, diffracted beams of any plane *hkl* form a diffraction cone. Therefore, intensity can be detected easily without the need of sample rotations or precise sample alignment and a moving point detector is sufficient to record all reflections.

CHAPTER 5: RESULTS

Before presenting the results, a new body-centered monoclinic axis system, called "2M," is introduced to describe the non-modulated structure. The monoclinic cell is half the size of the tetragonal unit cell and eases the interpretation of the TEM results. The relationship between the lattice parameters and unit cell orientation for the monoclinic (2M) and tetragonal (T) axis systems are given in Figure 5.1. From the tetragonal symmetry, it follows that in the monoclinic axis system, $a_{2M} = c_{2M}$, $b_{2M} = b_T$ and $c_{2M} = \frac{1}{2}\sqrt{{c_T}^2 + {a_T}^2}$. Results are given in both reference frames. Some important lattice planes and directions are listen in Table 5.1 for both axis systems.

Table 5.1 Important Lattice Planes and Directions for Tetragonal (T) and Monoclinic(2M) Axis Systems.

Tetragonal (T)	**Monoclinic (2M)**	**Tetragonal (T)**	**Monoclinic (2M)**
Plane (hkl)		**Direction (uvw)**	
$10\bar{1}$	100	$10\bar{1}$	100
010	010	010	010
101	001	101	001
220	121	$1\bar{1}1$	210
$\bar{2}2\bar{4}$	$12\bar{3}$	$00\bar{1}$	$10\bar{1}$

022	$\bar{1}21$		
$50\bar{7}$	$60\bar{1}$		
$40\bar{8}$	$60\bar{2}$		

The relationship between the planes and directions of the 2M and the tetragonal cells can be written as:

$$\begin{pmatrix} u \\ v \\ w \end{pmatrix}_{2M} = \mathbf{C} \begin{pmatrix} u \\ v \\ w \end{pmatrix}_{T} \tag{23}$$

$$(hkl)_{2M} = (hkl)_{T}\,\mathbf{C}^{-1} \tag{24}$$

$$\mathbf{C} = \begin{pmatrix} 1 & 0 & \bar{1} \\ 0 & 1 & 0 \\ 1 & 0 & 1 \end{pmatrix} \tag{25}$$

$$\mathbf{C}^{-1} = \frac{1}{2}\begin{pmatrix} 1 & 0 & 1 \\ 0 & 2 & 0 \\ \bar{1} & 0 & 1 \end{pmatrix} \tag{26}$$

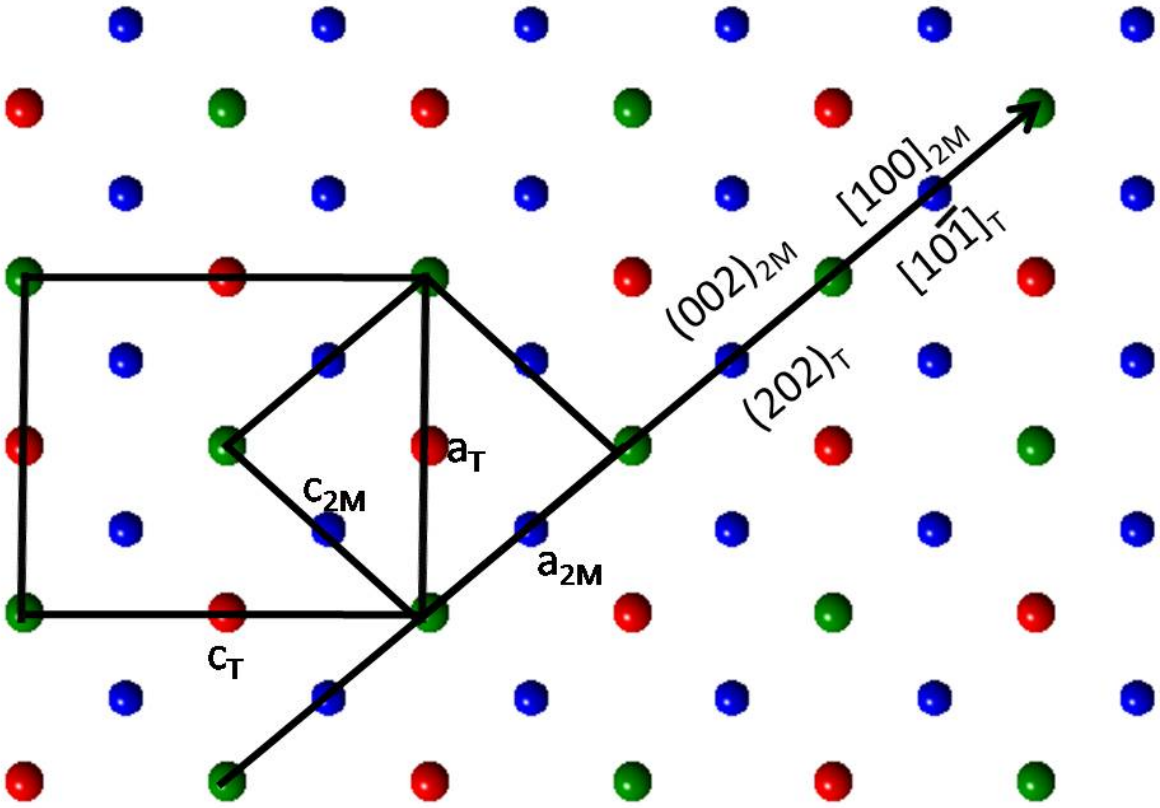

Figure 5.1 Relationship Between Face Cetered Tetragonal (T) Unit Cell and the New, Body-Centered Monoclinic Cell (2M).

5.1 XRD Results

X-ray diffraction experiments were first performed on bulk polycrystalline samples to ensure the material was in the non-modulated phase and to determine the lattice parameters. The diffracted x-ray intensity as a function of Bragg angle, 2θ, is shown in Figure 5.2, indexed according to the face-centered tetragonal axis system (indexed T) and the new, monoclinic axis system (indexed 2M).

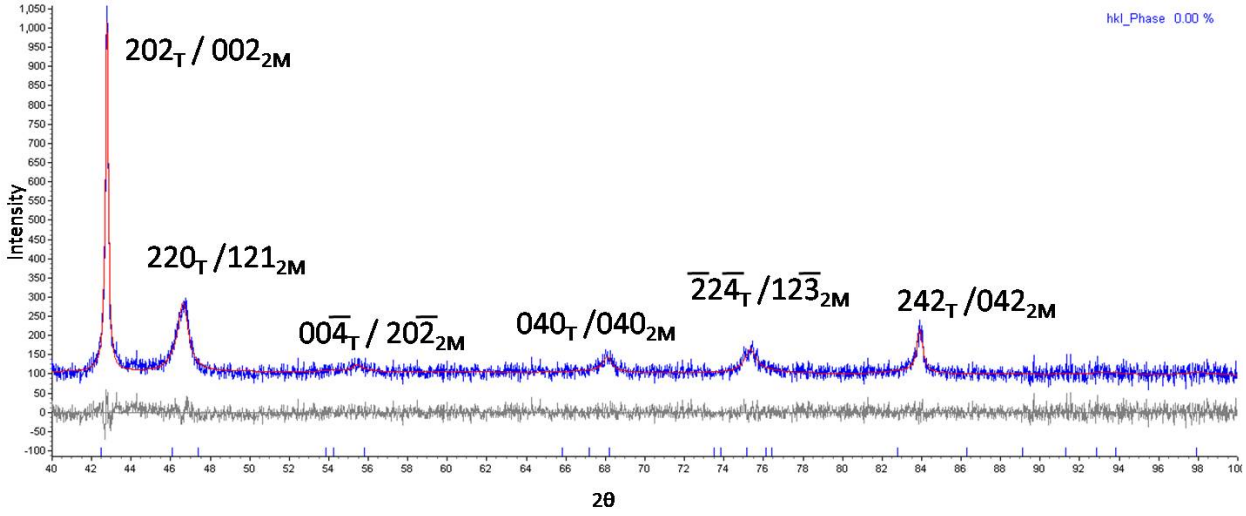

Figure 5.2 XRD of Bulk Polycrystalline Ni-Mn-Ga with Non-Modulated Martensite Structure. The Pattern Is Indexed According to the Face-Centered Tetragonal Axis System (T) and Body-Centered Monoclinic Axis System (2M).

The lattice parameters calculated for the tetragonal and monoclinic axis systems are given in Table 5.2. The tetragonal lattice parameters match well with those reported in Table 3.1.

Table 5.2 Lattice Parameters of the Non-Modulated Structure Measured with XRD for the Tetragonal and 2M Axis Systems.

Unit Cell	Lattice Parameters Å			Angles		
	a	*b*	*c*	*α*	*β*	*λ*
Face-Centered Tetragonal "T"	5.568	5.568	6.587	90	90	90
Body-Centered Monoclinic "2M"	4.313	5.568	4.313	90	99.58	90

5.2 TEM Results

Figure 5.3 is a bright-field image showing the typical morphology of the non-modulated martensite. Several different marensite variants are seen, with a high density

of nanotwins extending across an entire martensite plate. The inset diffraction pattern corresponds to the large martensite variant on the left, which is aligned along the $[210]_{2M}$/ $[1\bar{1}\bar{1}]_T$ zone axis. Some martensite variants intersect in a straight line, marked with "1", while other variants form jagged, stepped interfaces, marked with "2".

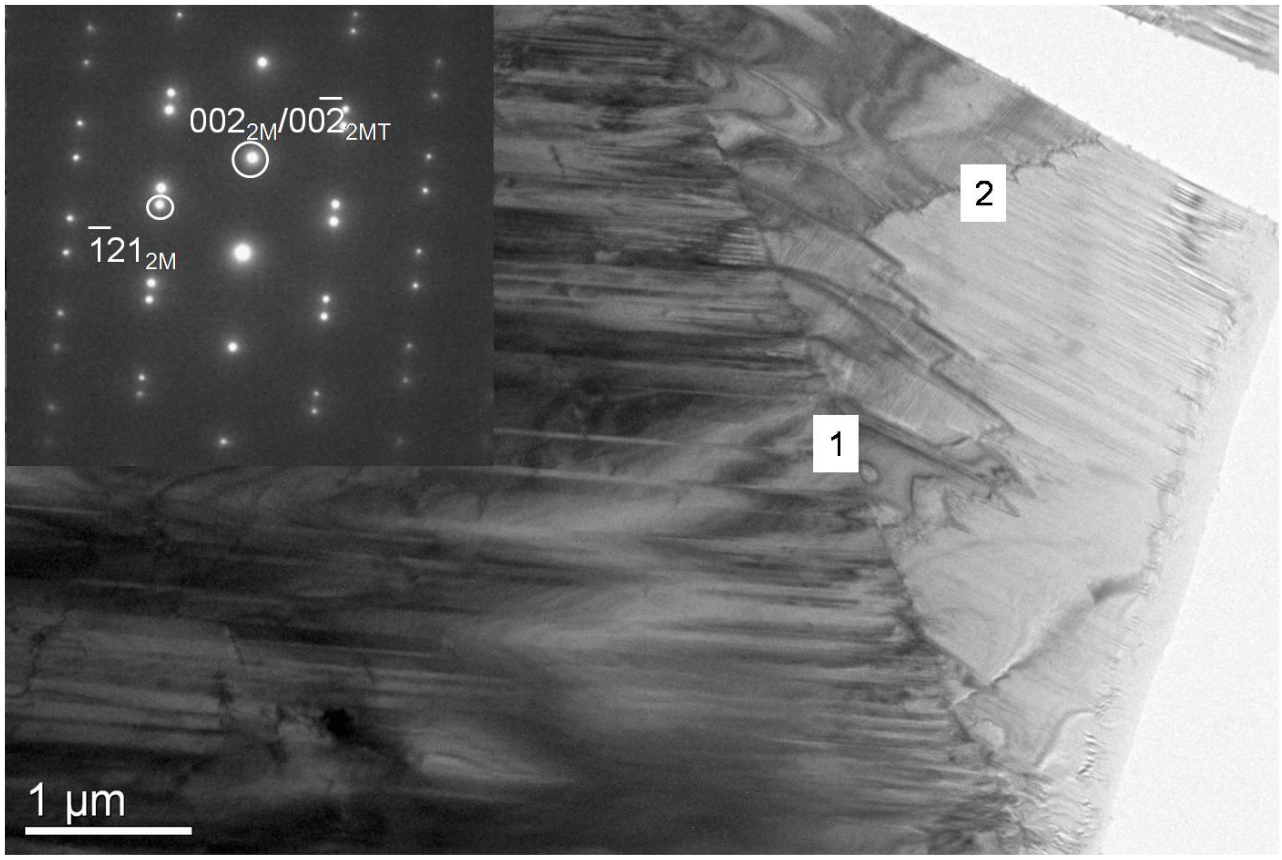

Figure 5.3 Bright-Field TEM Image Showing Multiple Martensitic Variants. Two Variants Meet in a Straight Line, Marked with "1", While Others Meet in a Jagged Boundary, Marked with "2". The Diffraction Pattern Corresponds to the Large Variant on the Left, Which Is Viewed Along the $[210]_{2M}/[1\bar{1}\bar{1}]_T$ Zone Axis.

Figure 5.4 shows location 1 at a higher magnification. Both martensite variants are aligned along the $[210]_{2M}/[1\bar{1}\bar{1}]_T$ zone axis. The corresponding diffraction pattern for each variant is inlayed in the image. Comparison of the diffraction patterns with the

bright-field image shows that the reflection of $(002)_{2M}/(202)_T$ is nearly perpendicular to the twin boundaries, indicating that $(001)_{2M}/(101)_T$ is the twin plane. The presence of thin plates on $(001)_{2M}/(101)_T$ is also evident from the streaking perpendicular to this diffraction spot. The diffraction pattern at the top of the image is taken over the center of both variants. The diffraction patterns are rotated approximately 60° from one another.

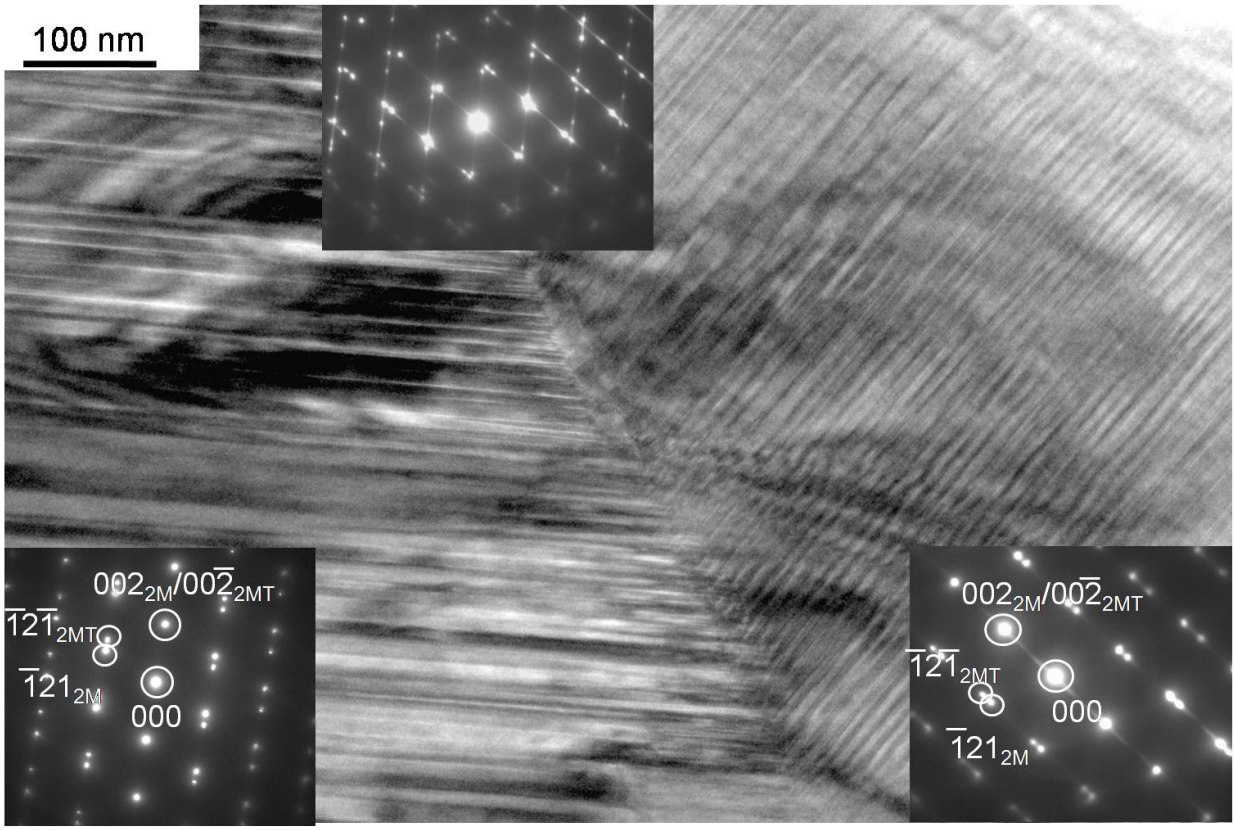

Figure 5.4 A Higher Magnification Image of Location 1. Both Martensitic Variants Are Aligned Along the $[210]_{2M}/[11\bar{1}]_T$ Zone Axis. The Corresponding Diffraction Patterns for Each Variant Are Inset in the Image. The Diffraction Pattern at the Top of the Image Is Taken over the Center of Both Variants.

The interface at "1" appears as a smooth, straight line in Figure 5.3. However, at higher magnification, Figure 5.4 shows that the interface actually undulates slightly. The density of internal twin variants in the left martensite variant of Figure 5.4 appears to change along the interface. The changing density of internal twins changes the exact

location of the interface, so that microscopically the interface is not a smooth line. The macroscopic variant interface is approximately $(\bar{1}21)_{2M} / (\bar{1}2\bar{1})_{2MT}$.

The $[210]_{2M}/[1\bar{1}\bar{1}]_T$ zone axis of the variants meeting at location 2 do not coincide. Instead, the sample was tilted to the $[010]_{2M}/[010]_T$ zone axis to obtain the bright field image shown in Figure 5.5. The diffraction pattern from each variant is inlayed in the top and bottom corners, along with the diffraction pattern of both variants in the top-right corner. Again, comparison of the diffraction patterns with the bright-field image shows that $(002)_{2M}/(202)_T$ is the twinning plane, and streaking corresponds to the thin plates on $(002)_{2M}/(202)_T$. The diffraction patterns of the two variants are rotated approximately 90° from each other. The interface is not a smooth line, as in location 1. Instead, it is stepped parallel and perpendicular to the $(002)_{2M}$ planes of the internal twins in both variants.

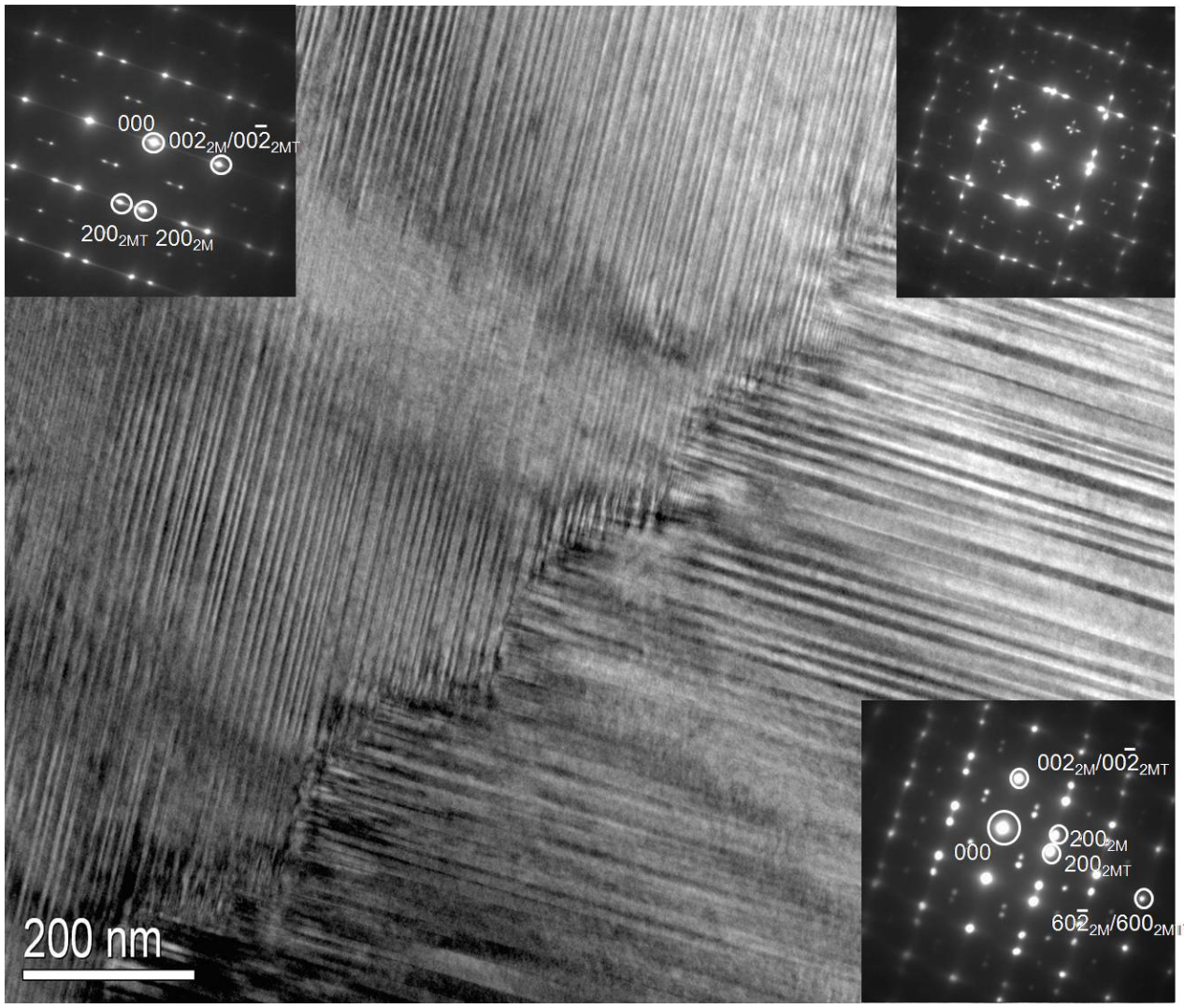

Figure 5.5 Location 2 Viewed Along the $[010]_{2M}$/[010]T Zone Axis. The Diffraction Pattern from Each Variant Is Inlayed, Along with the Diffraction Pattern of Both Variants. $(002)_{2M}$ Is the Twinning Plane. The Interface Is Not a Smooth Line, as in Location 1, But Steps Parallel and Perpendicular to the $(001)_{2M}$ Planes of the Internal Twins in Both Variants.

The remaining results focus on the interface at location 1. Figure 5.6 (a) and (b) are two complementary dark-field images of location 1, rotated by about 60° from Figure 5.3. The images were taken with the lower martensitic variant aligned along the $[210]_{2M}$/ $[1\bar{1}\bar{1}]_T$ axis. The aperture was displaced to circle the $(\bar{1}21)_{2M}$ reflection to create Figure

5.6 (a), and the twinned spot $(\bar{1}2\bar{1})_{2MT}$ was used to create Figure 5.6 (b). The twins are edge-on, with the twin density highest at the martensitic interface. The twins appearing bright in (a) appear dark in (b), and visa versa.

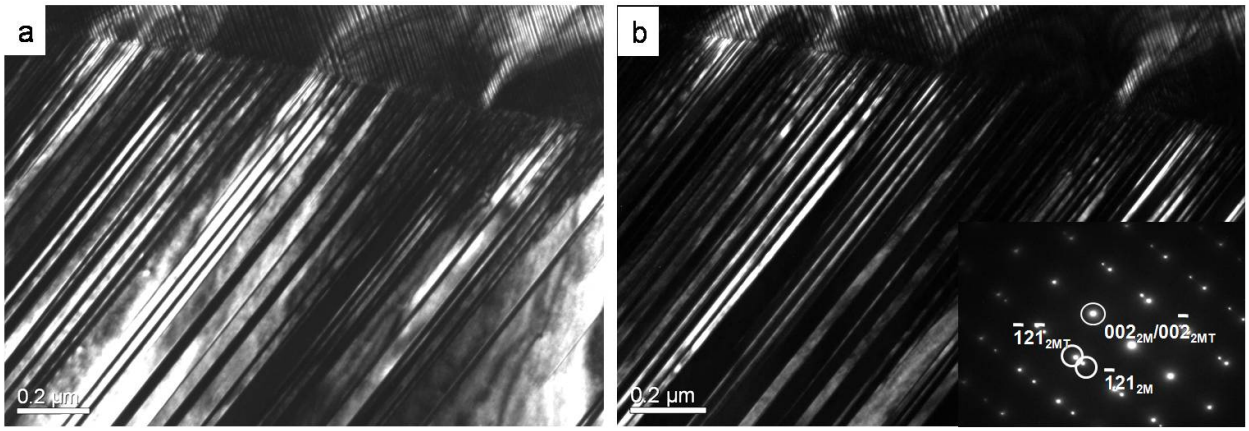

Figure 5.6 Complementary Dark Field Images of Location1 Viewed Along $[210]_{2M}$ Zone Axis So That the Twins Are Viewed Edge On. The Aperture Was Displaced to Select the $(\bar{1}21)_{2M}$ Spot for the Image on the Left, and the Twinned Spot $(\bar{1}2\bar{1})_{2MT}$ for the Image on the Right. The Density of Twins Is Highest at the Martensitic Interface.

Figure 5.7(a) shows a bright-field image of Location 1 in a two-beam condition with $\mathbf{g} = 202_{2M}/400_{T}$ near the zone axis $[10\bar{1}]_{2M}/[00\bar{1}]_{T}$. Away from the martensite interface, three levels of fringe contrast are distinguishable and occur in a regular sequence. Figure 5.7(b) shows the fringe contrast at higher magnification and Figure 5.7(c) is a schematic emphasizing the three types of contrast, which are two fringe patterns and a region without contrast.

Close to the martensite interface, the fringe contrast becomes undistinguishable. The twins are much finer and denser close to the interface, as seen in Figure 5.6. In the tilted view of Figure 5.7, many twin boundaries overlap, which confuses the contrast.

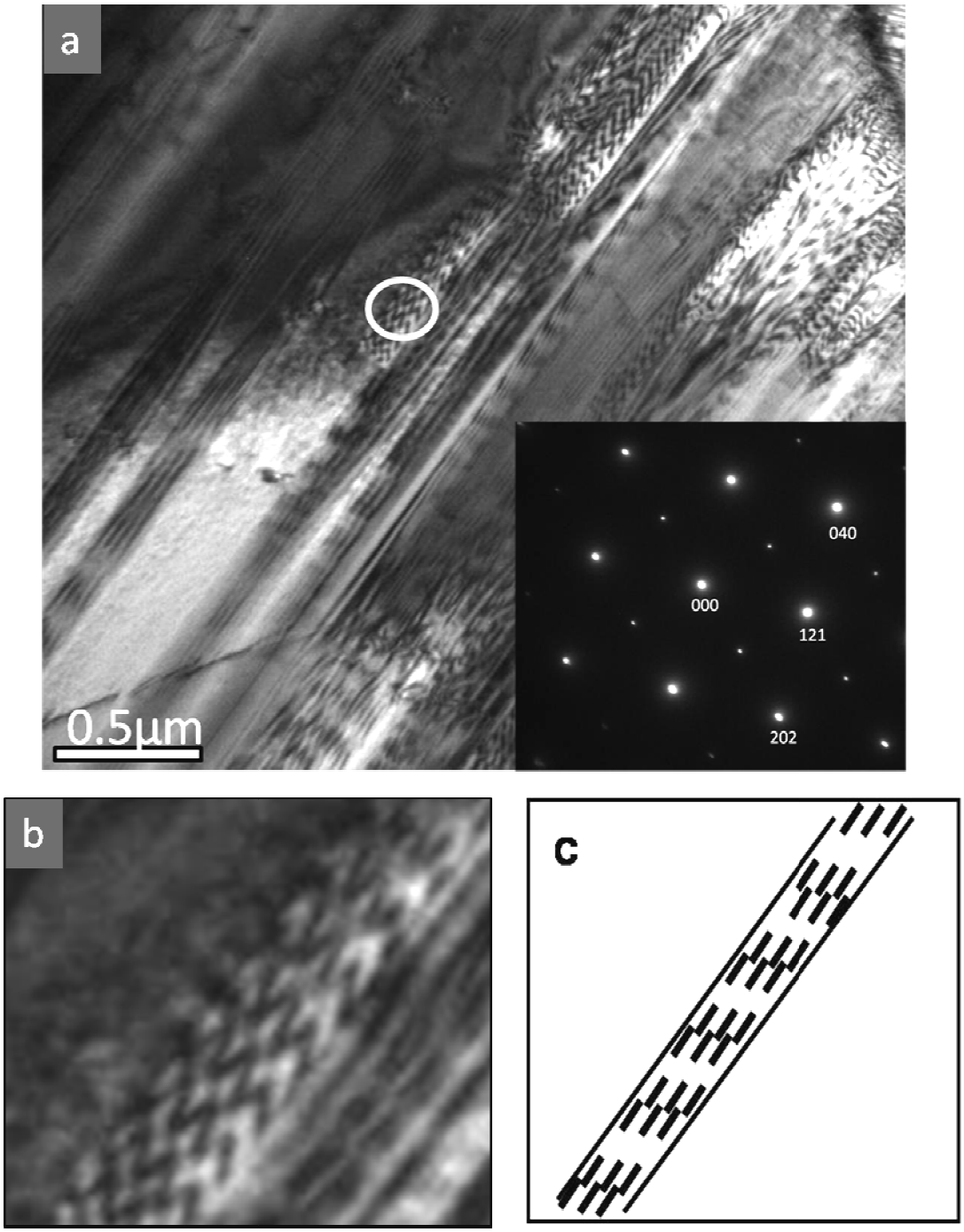

Figure 5.7 (a) Bright Field Image of Location 1 in a Two-Beam Condition with $g = (202)_{2M}/(400)_T$ Near the Zone Axis $[10\bar{1}]_{2M}/[00\bar{1}]_T$ (Diffraction Pattern Inserted). Away from the Martensite Interface, Three Levels of Fringe Contrast Are Distinguishable and Occur in a Regular Sequence. (b) Fringe Contrast at Higher Magnification. (c) Schematic Emphasizing the Three Types of Contrast.

Figure 5.8 is a bright-field image of the same location as Figure 5.7(a), in a two-beam condition with $\mathbf{g} = 040_{2M}/040_{T}$ near the zone axis $[10\bar{1}]_{2M}/[00\bar{1}]_{T}$. No fringe contrast is seen in this image.

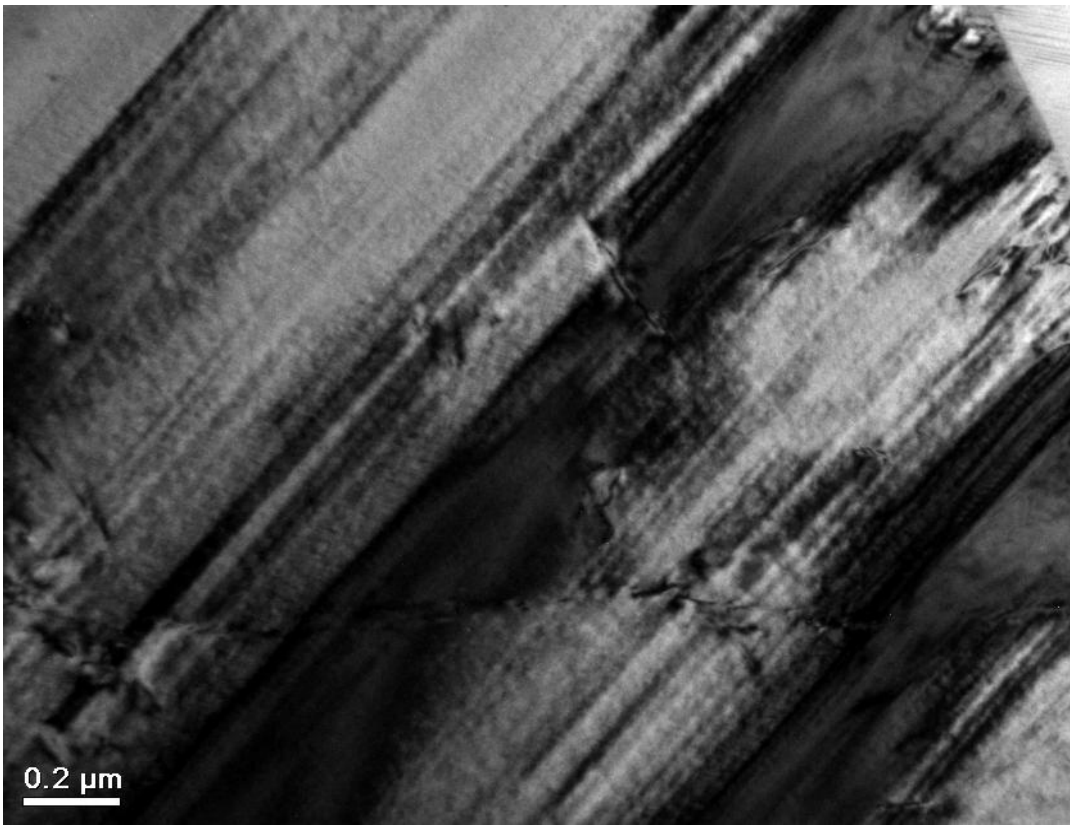

Figure 5.8 Bright-Field Image of Location 1 in a Two-Beam Condition with $g = (040)_{2M}/(040)_{T}$ Near the Zone Axis $[10\bar{1}]_{2M}/[00\bar{1}]_{T}$. No Fringe Contrast Is Seen.

CHAPTER 6: DISCUSSION

6.1 2M Twin Structure

The relationship between 2M and 2MT is determined to be the mirror operation parallel to the $(001)_{2M}$ plane. Thus, the axes of the 2MT cell form a left-handed set. The relationship between the 2M cell and its twin, 2MT, is shown schematically in Figure 6.1, where the unit cells are viewed along the $[010]_{2M}/[010]_{2MT}$ axis.

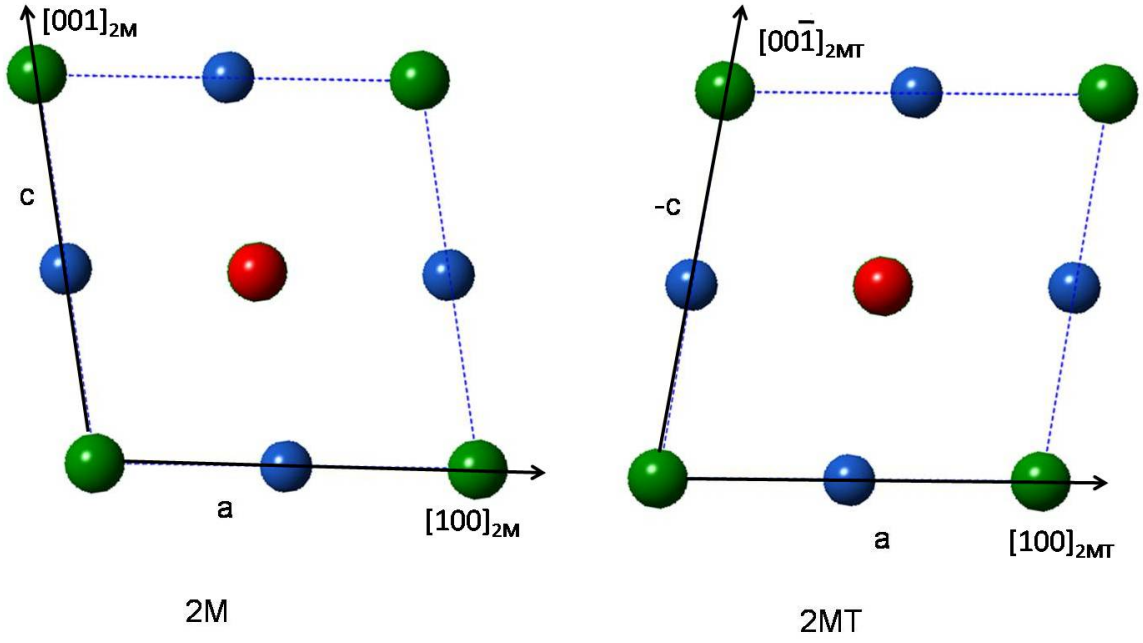

Figure 6.1 Relationship Between 2M and 2MT. The Viewing Direction Is Parallel to the $[010]_{2M}/[010]_{2MT}$.

The twin relation can be written as

$$(hkl)_{2MT} = (hkl)_{2M}\mathbf{P} \tag{27}$$

$$\begin{pmatrix} u \\ v \\ w \end{pmatrix}_{2MT} = \mathbf{P}^{-1} \begin{pmatrix} u \\ v \\ w \end{pmatrix}_{2M} \tag{28}$$

$$\mathbf{P} = \mathbf{P}^{-1} = \begin{pmatrix} 1 & 0 & -1/3 \\ 0 & 1 & 0 \\ 0 & 0 & -1 \end{pmatrix} \tag{29}$$

P is the transformation matrix used to turn the 2M axis system into the 2MT axis system. The determinant of **P** is -1, indicating that the right-handed axis system in 2M converts to a left-handed axis system in 2MT.

The twinning shear is described as $s = b/h$. The variables b and h are described in Figure 6.2, where the 2M and 2MT cells have been overlayed in the $[010]_{2M/2MT}$ direction. By geometry,

$$h = \frac{a}{2}\cos(\beta - 90) = \frac{a}{2}\sin\beta \tag{30}$$

$$b = a\sin(\beta - 90) = -a\cos\beta \tag{31}$$

$$\frac{b}{h} = 2\tan(\beta - 90) = -2\cot\beta \tag{32}$$

Using the lattice parameters presented in Table 5.1, $h = 2.13$Å, $b = 0.72$Å, and $s = 0.338$.

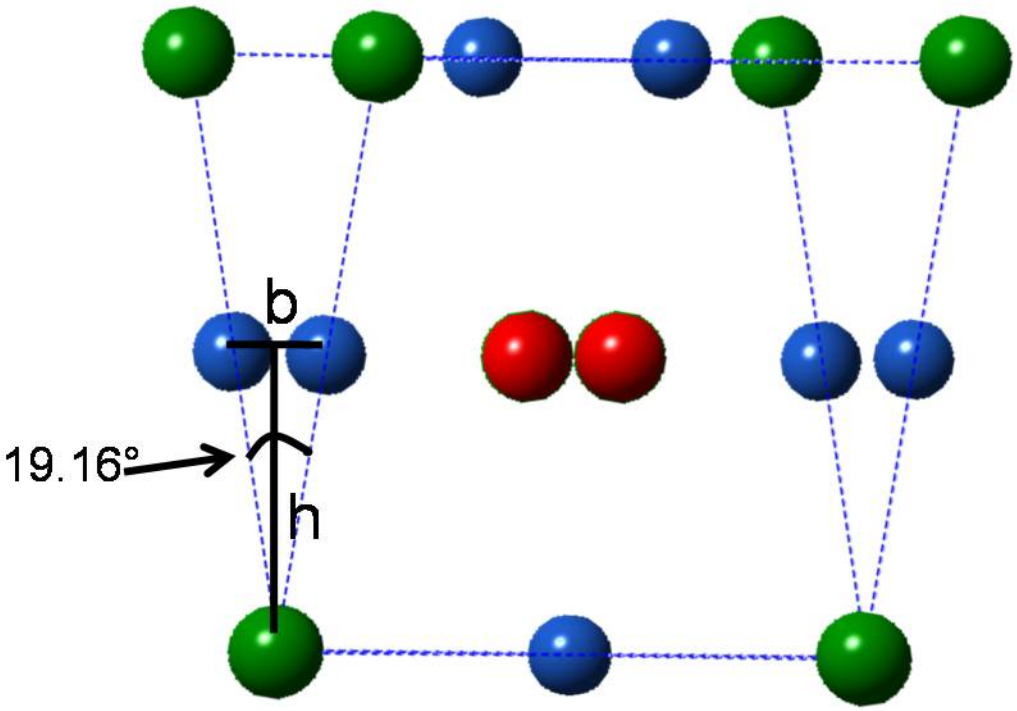

Figure 6.2 2M and 2MT Unit Cells Overlayed to Calculate Twinning Shear. Twinning Shear Is Defined as *b*/*h* and Is Found to be Approximately 1/3.

The diffraction pattern in the inlay of Figure 5.5, taken along the $[010]_{2M}$ zone axis, is reproduced in Figure 6.3 (a). The $60\bar{2}_{2M}$ reflection is coincident with the 600_{2MT} reflection. This is consistent with **b** = 1/6[100] and $h = d_{002}$. From $a_{2M} = c_{2M,}$ it follows that:

$$h = \frac{\sqrt{35}}{12} a \tag{33}$$

$$s = \frac{b}{h} = \frac{2}{\sqrt{35}} = 0.338 \tag{34}$$

Figure 6.3(b) demonstrates the relationship between the 2M and 2MT cells and the coincidence of the $60\bar{2}_{2M}$ and 600_{2MT} planes (dashed green lines). The $(60\bar{1})_{2M/2MT}$ planes are coincident for both lattices (shown as blue dash-dotted lines).

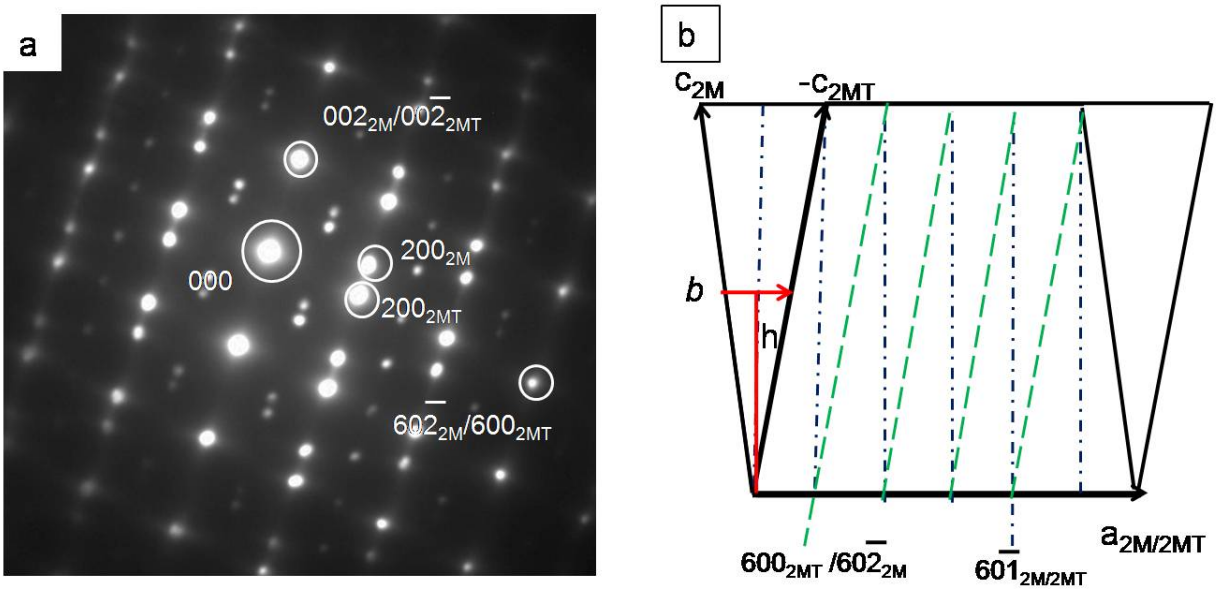

Figure 6.3 (a) SADP Showing the Coincidence of 600_{2MT} and $60\bar{2}_{2M}$. (b) Schematic Demonstrating the Coincidence of 600_{2MT} and $60\bar{2}_{2M}$ (Green Dashed Lines), and $(60\bar{1})_{2M/2MT}$ (Blue Dashed Lines). This Is Consistent with b = 1/6[100] and h = d_{002}.

6.2 Martensite Interfaces

Two types of martensite variant boundaries are seen in Figure 5.4. The habit plane of the twins within each variant is $(001)_{2M}/(101)_T$. The martensite variants themselves are related to the habit planes $(\bar{1}21)_{2M}/(022)_T$. These two types of plane are demonstrated schematically in Figure 6.4 for the tetragonal unit cell. In this figure, the $(101)_T/(001)_{2M}$

twin plane is shown in blue and the $(022)_T/(\bar{1}21)_{2M}$ habit plane of the martensite variants is shown in red. Figure 6.4(a) shows the tetragonal unit cell in a random orientation, and (b) shows the unit cell viewed along the $[11\bar{1}]_T$ /$[210]_{2M}$ direction. The planes make an angle of approximately 65.37º with one another.

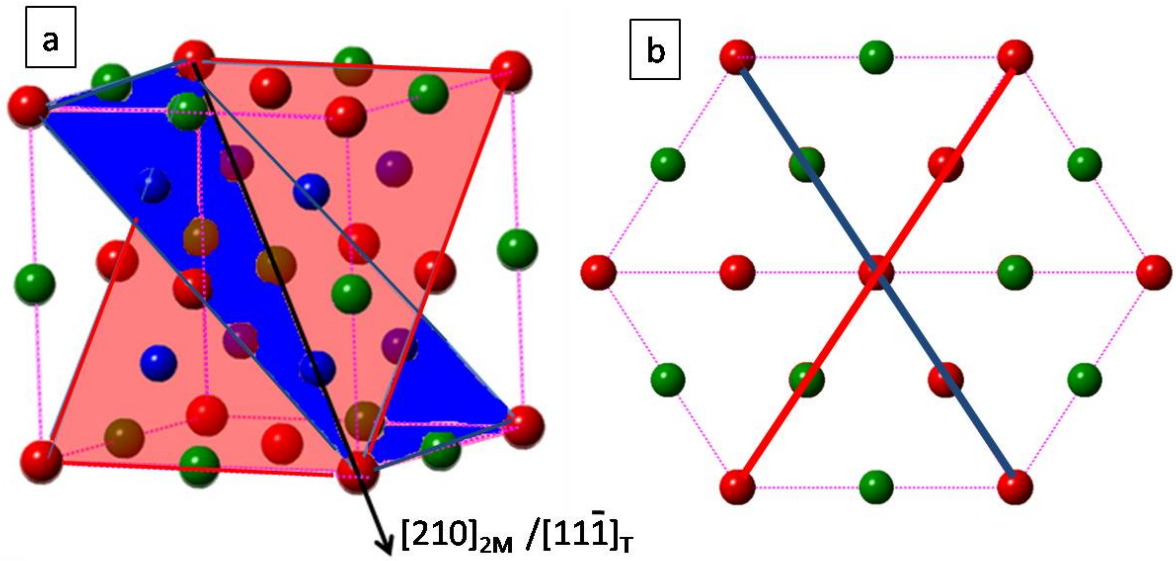

Figure 6.4 (a) Tetragonal Unit Cell Showing the $(101)_T/(001)_{2M}$ Twin Plane in Red and $(022)_T/(\bar{1}21)_{2M}$ Habit Plane in Blue. (b) Tetragonal Unit Cell Viewed in the $[11\bar{1}]_T/[210]_{2M}$ Direction Showing the $(101)_T/(001)_{2M}$ Twin Plane in Red and $(002)_T/(\bar{1}21)_{2M}$ Habit Plane in Blue.

Figure 5.5 shows the twins within each variant again with the habit plane $(001)_{2M}/(101)_T$; however, the microscopic habit plane for the martensite variants is $(100)_{2M}/(10\bar{1})_T$. The steps and associated planes are demonstrated schematically in Figure 6.5.

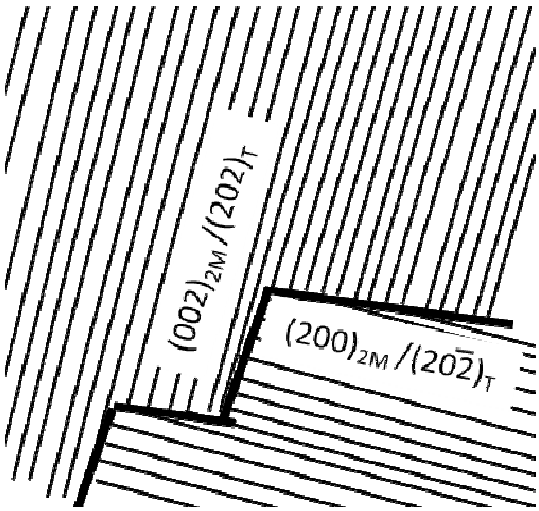

Figure 6.5 Schematic Demonstration of Steps in Rough Interface of Location 2 in Figure 5.5. Internal Twins Have Habit Plane $(001)_{2M}/(101)_T$ with $(100)_{2M}/(10\bar{1})_T$ Steps.

These planes are demonstrated in Figure 6.6, where the $(10\bar{1})_T/(100)_{2M}$ habit plane is shown in blue and the $(101)_T/(001)_{2M}$ twin plane in red. Figure 6.6 (a) views the tetragonal unit cell in a random direction, and (b) views the cell in the $[010]_T/[010]_{2M}$ direction. The planes make an angle of approximately 80.42º with one another.

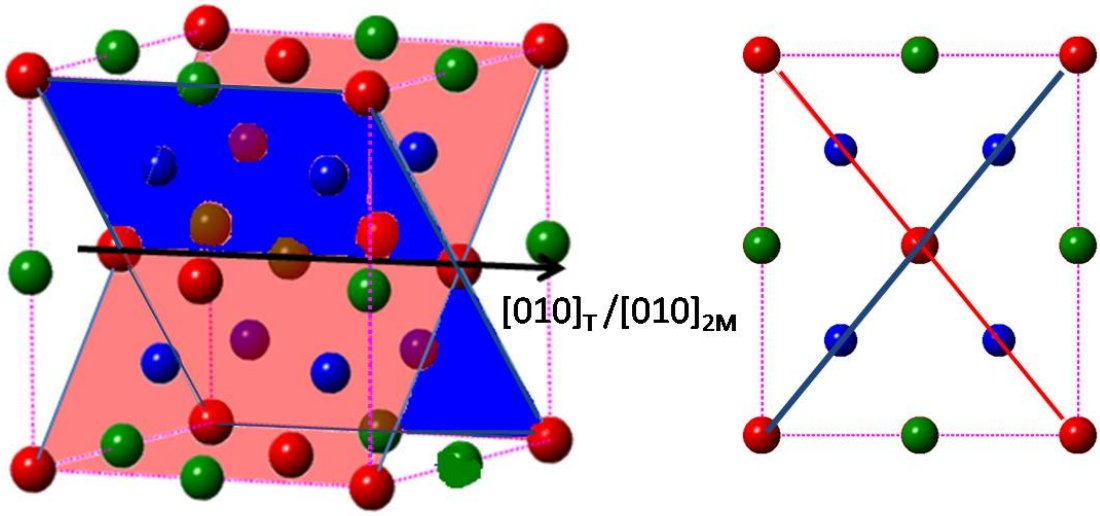

Figure 6.6 (a) Tetragonal Unit Cell Showing the $(10\bar{1})_T$ / $(100)_{2M}$ Habit Plane in Blue and $(101)_T$/$(001)_{2M}$ Twin Plane in Red. (b) Tetragonal Unit Cell Viewed in the $[010]_T$/$[010]_{2M}$ Direction Showing the $(10\bar{1})_T$ / $(001)_{2M}$ Habit Plane in Blue and $(101)_T$/$(001)_{2M}$ Twin Plane in Red.

The interface at location 1 in Figure 5.3 was seen to be slightly undulated at higher magnifications. The martensite variant on the left has varying twin densities, which will control the exact position of the boundary. The variant on the right has constant densities of twins. These twins do not coarsen probably because they are sandwiched between two martensite variants. If they were to coarsen, the elastic energy at the jagged interface would be high.

6.3 Twin Branching

The phenomenological theory of martensite [35] predicts a periodic twinning of the non-modulated tetragonal martensite lattice, expressed through the fraction of the twin lamella widths d_1 and d_2 : $d_1/d_2 = (a_{2M}\text{-}a_A)/(a_A\text{-}c_{2M})$. The subscript 'A' is used to denote the lattice parameters of the austenite phase. The lattice parameters obtained with

XRD (Table 5.2) give a twinning periodicity of $d_1/d_2 = 0.337$. When considering the 14M structure with a $(\bar{5}2)_2$ stacking sequence, the ideal value of $d_1/d_2 = 2/5 = 0.4$. The ideal ratio for the 14M structure is close to the ratio seen for the non-modulated structure. This suggests that the 14M modulated structure and a microscopic 2M structure may be related [56].

One of the dark-field images from Figure 5.6 (a) is reproduced in Figure 6.7. A straight line was drawn close to the martensite boundary crossing nineteen twin boundaries. A distance away from the boundary, a line of equal length was drawn that only crosses eleven twin boundaries. Further away, the same line crosses eight, and even further away crosses only four twin boundaries. The number fraction of twins is significantly higher at the martensite interface, which is consistent with the branching of twins described by Kohn and Müller [29]. The same procedure can be done with the dark-field image from the corresponding twin, which gives the same results.

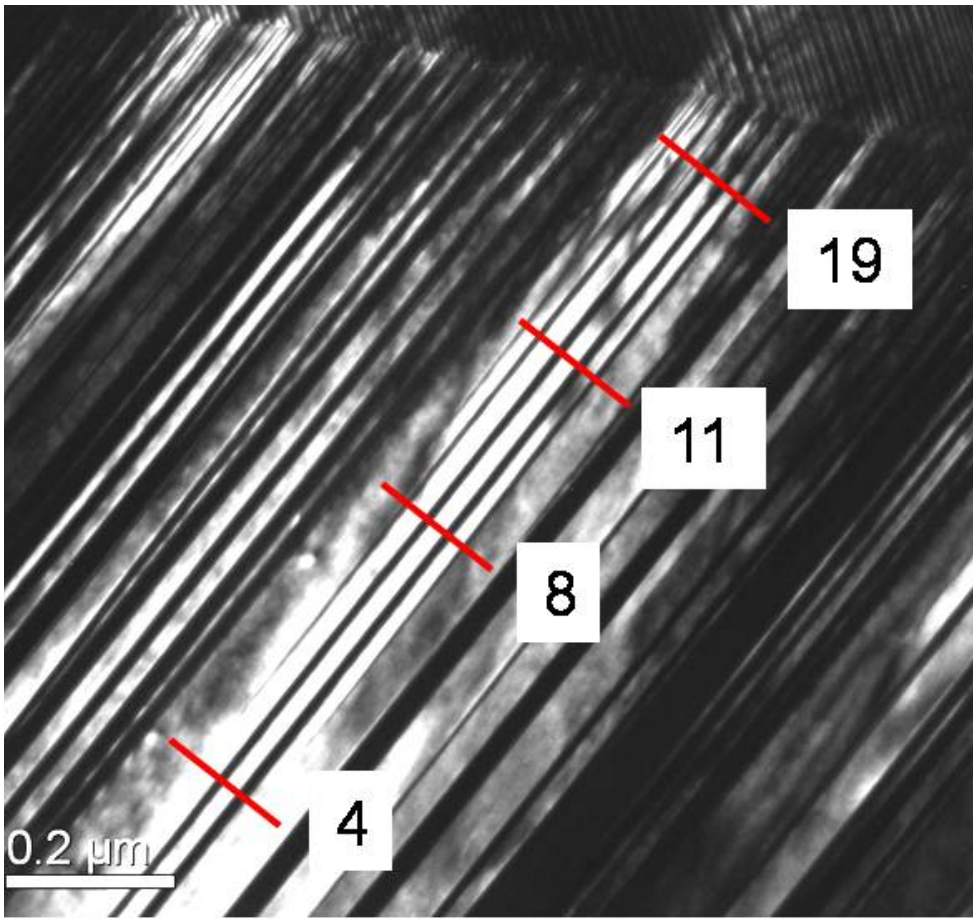

Figure 6.7 Dark Field Image Showing the Branching of Twins Near a Martensite Boundary. Close to the Boundary a Line Is Drawn That Crosses 20 Twins. Further Away the Same Line Is Drawn That Now Crosses Only 12 Twins, then 9, then 5. This Is Consistent with Twin Branching.

This branching is shown schematically in Figure 6.8, where some thick twins continue through the martensite variant, but many fine twins terminate close to the martensitic variant boundary. The location circled will be discussed in detail in Section 6.5.

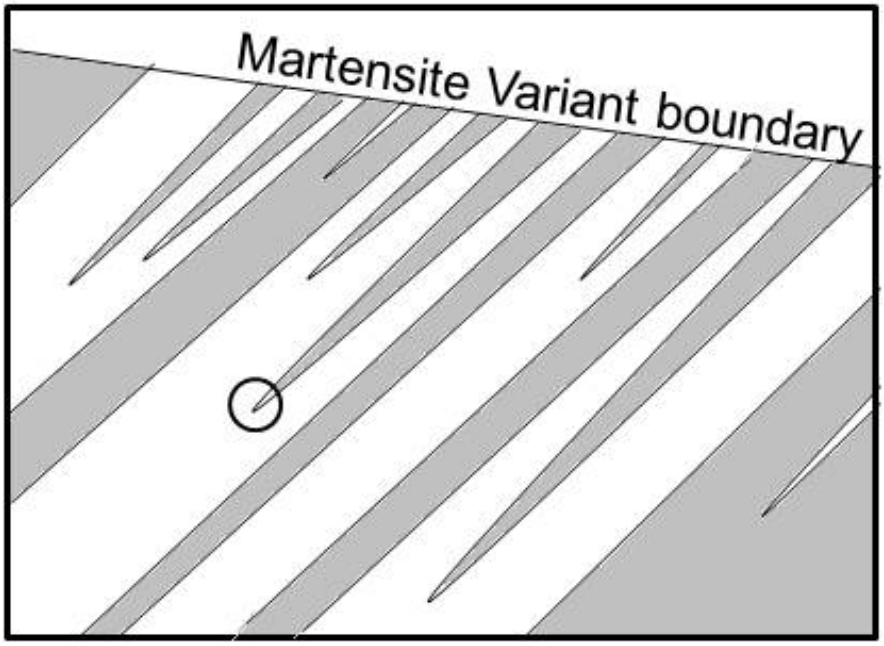

Figure 6.8 Schematic Illustration of Twin Branching. Some Thick Twins Continue Through the Martensite Variant, but Many Fine Twins Terminate Close to the Martensitic Variant Boundary.

Branching of the non-modulated structure may not always be limited to the martensitic boundaries, but could occur across the whole of the martensitic plate due to geometrical constraints such as other martensitic plates, compositional influences, etc. If the non-modulated unit cell branched into full martensitic plates of nano-sized twins with d_1/d_2=0.4, the 14M structure could be built [56]. The key requirement for this branching is a low twin boundary energy [29]. The twin boundary energy obtained from the transformation enthalpy from 14M to 2M is 0.5 meV/Å^2 [57], fulfilling this key requirement.

6.4 Formation of 14M Structure

The 14M unit cell can be built from building blocks of non-modulated unit cells stacked in a specific sequence to give the $\bar{5}2$ stacking. This is envisaged using the non-

modulated monoclinic cell in Figure 6.9. An example monoclinic cell and its twin are outlined in red and the twinning planes are shown by dashed lines.

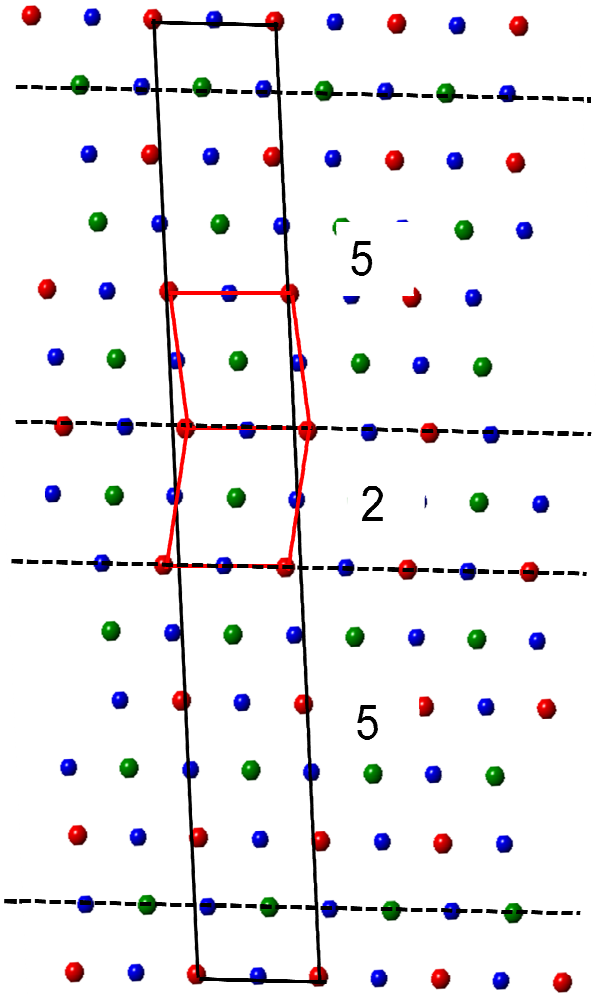

Figure 6.9 The 14M Unit Cell Built from Building Blocks of Non-Modulated Unit Cells An Example Monoclinic Cell and Its Twin Are Outlined in Red and the Twinning Planes Are Shown by Dashed Lines.

Using the lattice parameters for the monoclinic cell calculated from XRD results, the lattice parameters of the 14M unit cell composed of nanotwins of non-modulated unit

cells can be calculated. The results are shown in Table 6.1, along with lattice parameters for the 14M structure obtained from XRD for an alloy with composition $Ni_{54.3}Mn_{20.5}Ga_{25.2}$ [38] .

Table 6.1 Lattice Parameters for the 14M Structure (Monoclinic Cell) Calculated by Building the 14M Structure with Periodic Stacking of the 2M and the Lattice Parameters Seen Experimentally.

	a (nm)	b (nm)	c (nm)	β (°)
Calculated $Ni_{46.75}Mn_{34}Ga_{19.25}$	0.431	0.556	2.984	94.14
Experimental [38] $Ni_{54.3}Mn_{20.5}Ga_{25.2}$	0.426	0.543	2.954	94.3

The calculated values are in close agreement with those seen experimentally. The difference may be due to difference in composition. This suggests that the 14M structure can be created by branching of the non-modulated structure.

The same procedure can be used to build the 10M structure with a $(\bar{3}2)_2$ stacking sequence. The calculated lattice parameters when the 10M cell is built out of non-modulated cells along with the lattice parameters seen experimentally are shown in Table 6.2.

Table 6.2 Lattice Parameters for the 10M Structure (Monoclinic Cell) Calculated by Building the 10M Structure with Periodic Stacking of the 2M and the Lattice Parameters Seen Experimentally.

	a (nm)	b (nm)	c (nm)	β (°)
Calculated $Ni_{46.75}Mn_{34}Ga_{19.25}$	0.431	0.556	2.128	91.93
Experimental [38] $Ni_{51.5}Mn_{23.6}Ga_{24.9}$	0.424	0.566	2.05	90.5

The calculated values are not in as good of agreement to the experimental values for the 10M structure as they are for the 14M structure. The β angle predicted for the 10M cell is 1.43° larger than found experimentally. This does not rule out the possibility of the non-modulated structure branching to form the 10M structure; however, it suggests that other factors may play a role. The d_1/d_2 ratio for the ideal $(\bar{3}2)_2$ stacking ratio is 2/3 = 0.667. This is significantly larger than the ratio of 0.337 found for the non-modulated twins. The non-modulated structure could not simply branch into nano-twins but would have to change its twinning ratio to create the 10M cell.

Upon cooling and with increasing stress the austenite phase changes to a 10M then 14M and then non-modulated phase or to 14M and then non-modulated or directly from the austenite to the non-modulated phase [44]. This transformation sequence suggests that the 14M structure is more closely related to the non-modulated structure than the 10M structure, since a direct transformation from 10M to 2M has not been observed.

There is currently debate about the nature of the stacking of atomic planes in the 10M unit cell. It is possible that a periodical shuffling of the basal planes occurs, the displacement of each plane from its original position is given by a function containing harmonic terms [38]. If this is the case, then the non-modulated structure could not simply branch to form the 10M structure. Instead, a period shuffling of atoms would be necessary.

6.5 Fringe Contrast

The α fringe contrast seen in Figure 5.7 is typical of stacking fault contrast (see Section 4.2.2 Stacking Faults). Three types of fringe contrast indicate three types of stacking sequences in a regular, repeating pattern. Close to the interface it becomes difficult to distinguish the contrast. This is due to the branching of twins seen in Figure 6.4. Close to the martensitic interface the twins are much finer and denser, such that twin boundaries overlap in the titled view of Figure 5.7.

Figure 6.10 is a schematic of a tip of a twin containing twinning dislocations on each $(001)_{2M}/(101)_{T}$ plane emphasizing the 2M structure, while Figure 6.11 emphasizes the tetragonal structure. The 2M unit cell is shown in blue, with a green twin 2MT growing into the matrix. The straight grey lines represent the $(60\bar{1})_{2M}/(60\bar{1})_{2MT}/(50\bar{7})_{T}$ planes, which are coincident for the 2M and 2MT twins (Figure 6.3 (b)). The Burgers vectors are $\frac{1}{6}[100]_{2M}/\frac{1}{6}[100]_{2MT}/\frac{1}{12}[10\bar{1}]_{T}$, which are represented with red dislocation symbols.

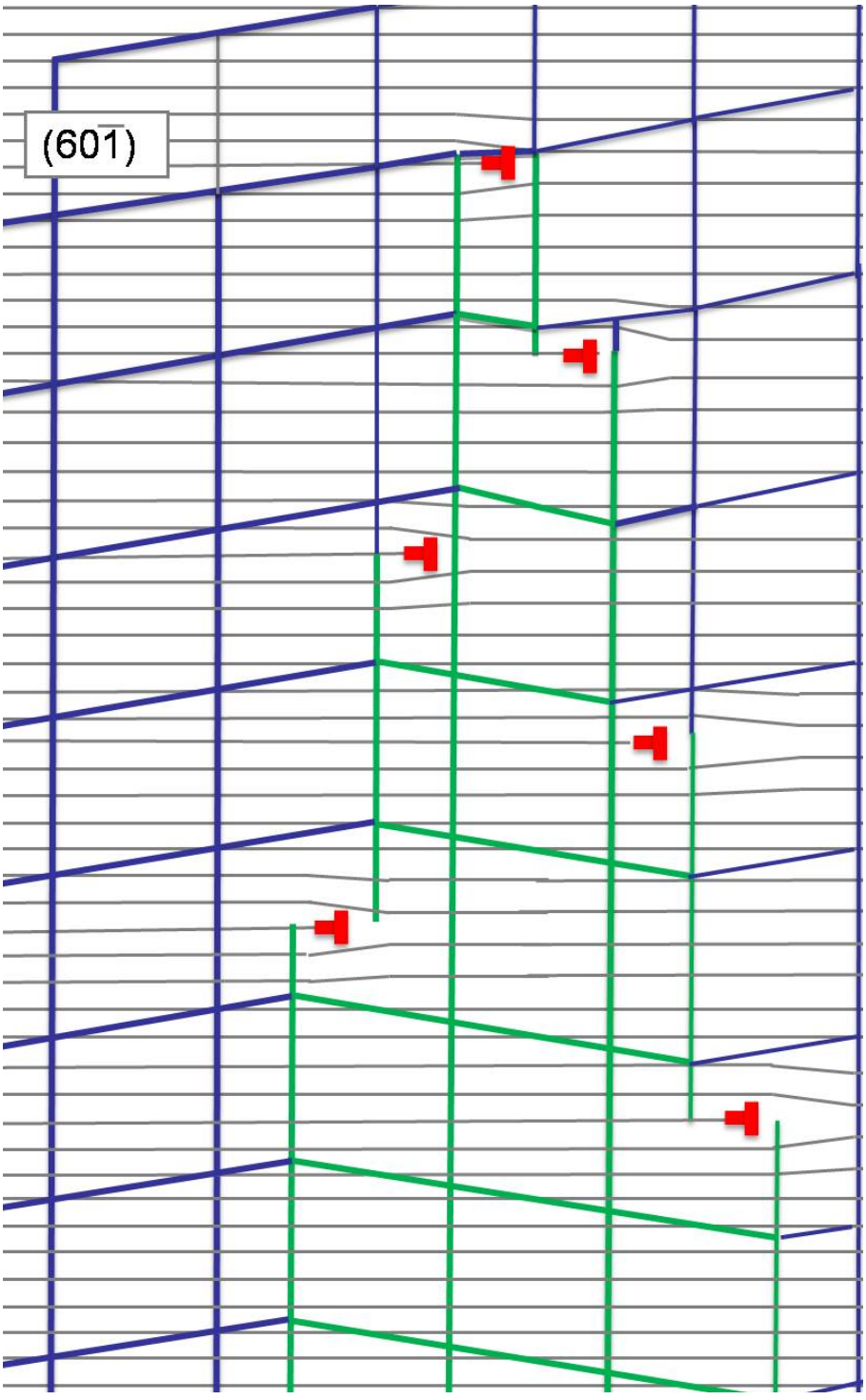

Figure 6.10 Schematic of a Twin Tip. 2M and 2MT Unit Cells Are Shown in Blue and Green. Dislocations Are Drawn on Each $(001)_{2M}$ Plane with b = $1/6[100]_{2M}$ = $1/6[100]_{2MT}$.

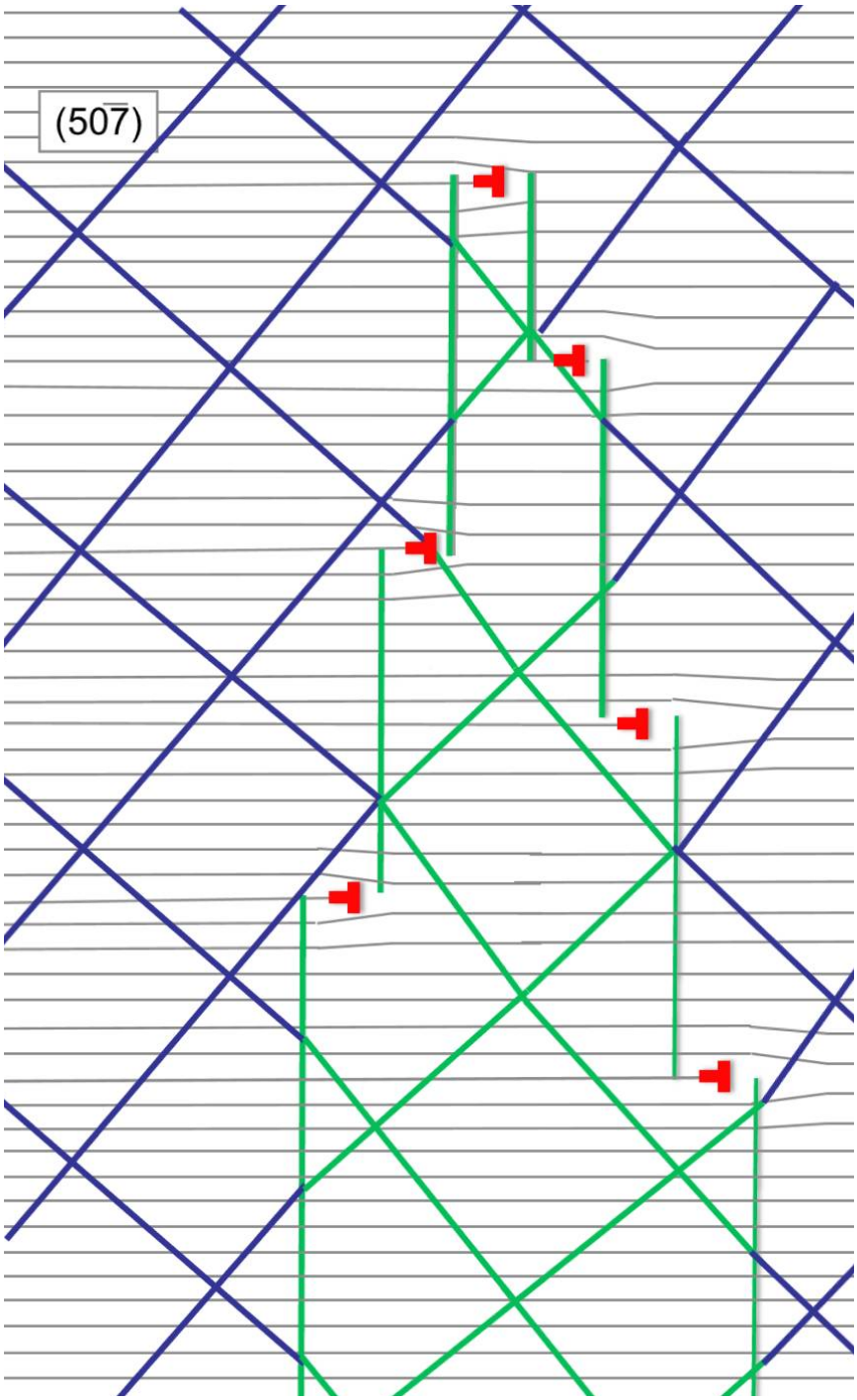

Figure 6.11 Schematic of a Twin Tip. Tetragonal Unit Cell and Its Twin Are Shown in Blue and Green. Dislocations Are Drawn on Each $(101)_T$ Plane with b = $1/12[10\bar{1}]_T$.

The growth of a twin in non-modulated Ni-Mn-Ga can be described by the movement of dislocations with burgers vector **b**= $\frac{1}{6}[100]_{2M}/\frac{1}{6}[100]_{2MT}$ on each successive $(001)_{2M}/(001)_{2MT}$ plane. The movement of such twinning dislocations will produce a change in the stacking sequence. At the first twinning dislocation, the matrix above the twin is displaced by a vector $\frac{1}{6}[100]_{2M}/\frac{1}{6}[100]_{2MT}$ relative to the matrix below the twin. Assuming the green twin is not in a diffraction condition, this will result in α fringe stacking-fault contrast. Similarly, the second disconnection produces a displacement of $\frac{1}{6}[100]_{2M} + \frac{1}{6}[100]_{2M} = \frac{1}{3}[100]_{2M}$. The third twining dislocation produces a displacement $\frac{1}{2}[100]_{2M}/\frac{1}{2}[100]_{2MT,}$ which is a lattice vector and will therefore produce no stacking fault contrast.

The operative reflection used to produce the fringe contrast in Figure 5.7 was **g** = 202_{2M}. Using a Burgers vector of $\frac{1}{6}[100]_{2M}$, a train of six twinning disconnections will result in $2\pi\mathbf{g}\bullet\mathbf{b}$ values of $2\pi(1/3, 2/3, 1, 1/3, 2/3, 1)$, hence three levels of fringe contrast [58]. If the product $\mathbf{g}\cdot\mathbf{b}$ is zero or an integer, then the crystal containing the stacking fault will give contrast identical to that from a perfect crystal [53]. For this system, every third fringe results in an integral α value, resulting in no fringe contrast. No fringe contrast can be seen in the twins in Figure 5.8. In this case, **g**=040, so that, if **b**=$\frac{1}{6}[100]_{2M,}$, then $\mathbf{g}\cdot\mathbf{b}=0$, resulting in no α fringe contrast.

The periodic pattern of fringe contrast, with every third dislocation resulting in no contrast, proves the perfect coincidence of the $60\bar{2}_{2M}/600_{2MT}$ planes and the Burgers vector of exactly $\frac{1}{6}[100]_{2M}/\frac{1}{6}[100]_{2MT}$. The repeating pattern of contrast requires that the Burgers vector have a rational relationship with the lattice parameter.

The dislocations themselves cannot be seen in Figure 5.7. The rule of thumb for visibility of partial dislocations is that a partial dislocation is visible if $\mathbf{g}\cdot\mathbf{b} > 1/3$. In this case, $\mathbf{g} = (202)_{2M,}$ $\mathbf{b} = \frac{1}{6}[100]_{2M}$, so $\mathbf{g}\cdot\mathbf{b} = 1/3$. These partial dislocations do not create enough distortion in the lattice to create dislocation contrast.

CHAPTER 7: OUTLOOK

The research presented in this thesis was performed to characterize the twinning microstructure of the non-modulated martensite. Twinning dislocations present between twin interfaces were studied in terms of their Burgers vectors and step heights; however, there is still much work to be done to fully characterize the defect content of the material. The defects present at the martensite interfaces should be characterized in terms of disclinations. Such a study will be useful for understanding and modeling the motion of twins in hierarchically twinned structures. In-situ transmission electron microscopy experiments in which hierarchically twinned martensite is strained enough to cause twin-boundary motion would also be useful in understanding the mechanisms of twin-boundary motion.

The non-modulated martensite structure was used to construct the modulated structures via branching into nano-twins. While this worked well for the 14M structure, the lattice parameters predicted for the 10M structure deviated significantly from those seen experimentally. Further research is necessary to understand the relationship between the 2M, 14M, and 10M structures and the transformation process from one structure to the other.

The non-modulated structure is known to have significantly higher twinning stresses than the modulated structures [8, 45, 51]. In order to understand the reasons for higher twinning stresses, a study similar to this should be conducted on both modulated

phases that characterize the types of defects present and the stresses associated with twin-boundary motion in each phase. This will allow more precise engineering control over the amount of strain a sample produces in a magnetic field.

REFERENCES

[1] D. Lagoudas, *Shape Memory Alloys: Modeling and Engineering Applications*. College Station: Springer, 2008.

[2] *Shape Memory Materials*. Cambridge: Cambridge University Press, 1998.

[3] V. A. Chernenko, E. Cesari, V. V. Kokorin, and I. N. Vitenko, "The Development Of New Ferromagnetic Shape-Memory Alloys In Ni-Mn-Ga System," *Scripta Metallurgica Et Materialia,* vol. 33, pp. 1239-1244, Oct 1995.

[4] K. Ullakko, J. K. Huang, C. Kantner, R. C. Ohandley, and V. V. Kokorin, "Large magnetic-field-induced strains in Ni2MnGa single crystals," *Applied Physics Letters,* vol. 69, pp. 1966-1968, Sep 1996.

[5] S. J. Murray, M. Marioni, S. M. Allen, R. C. O'Handley, and T. A. Lograsso, "6% magnetic-field-induced strain by twin-boundary motion in ferromagnetic Ni-Mn-Ga," *Applied Physics Letters,* vol. 77, pp. 886-888, Aug 2000.

[6] P. Mülner, V. A. Chernenko, M. Wollgarten, and G. Kostorz, "Large cyclic deformation of a Ni-Mn-Ga shape memory alloy induced by magnetic fields," *Journal of Applied Physics,* vol. 92, pp. 6708-6713, Dec 2002.

[7] A. Sozinov, A. A. Likhachev, N. Lanska, and K. Ullakko, "Giant magnetic-field-induced strain in NiMnGa seven-layered martensitic phase," *Applied Physics Letters,* vol. 80, pp. 1746-1748, Mar 2002.

[8] P. Müllner, V. A. Chernenko, and G. Kostorz, "Large cyclic magnetic-field-induced deformation in orthorhombic (14M) Ni-Mn-Ga martensite," *Journal of Applied Physics,* vol. 95, pp. 1531-1536, Feb 2004.

[9] R. C. O'Handley, S. J. Murray, M. Marioni, H. Nembach, and S. M. Allen, "Phenomenology of giant magnetic-field-induced strain in ferromagnetic shape-memory materials (invited)," *Journal of Applied Physics,* vol. 87, pp. 4712-4717, May 2000.

[10] K. Ullakko, "Magnetically controlled shape memory alloys: A new class of actuator materials," *Journal of Materials Engineering and Performance,* vol. 5, pp. 405-409, Jun 1996.

[11] *Encyclopedia of Smart Materials* vol. 2. New York: John Wiley and Sons, Inc., 2002.

[12] G. H. Haertling, "Ferroelectric ceramics: History and technology," *Journal of the American Ceramic Society,* vol. 82, pp. 797-818, Apr 1999.

[13] S. A. Wilson, R. P. J. Jourdain, Q. Zhang, R. A. Dorey, C. R. Bowen, M. Willander, Q. U. Wahab, M. A. H. Safaa, O. Nur, E. Quandt, C. Johansson, E. Pagounis, M. Kohl, J. Matovic, B. Samel, W. van der Wijngaart, E. W. H. Jager, D. Carlsson, Z. Djinovic, M. Wegener, C. Moldovan, R. Iosub, E. Abad, M. Wendlandt, C. Rusu, and K. Persson, "New materials for micro-scale sensors and actuators An engineering review," *Materials Science & Engineering R-Reports,* vol. 56, pp. 1-129, Jun 2007.

[14] J. Ahola, T. Liedes, P. Kroneld, and K. Nevala, "On magnetic shape memory alloy actuator characteristics," *Journal of Vibroengineering,* vol. 11, pp. 443-449, Sep 2009.

[15] E. Asua, J. Feuchtwanger, A. Garcia-Arribas, V. Etxebarria, I. Orue, and J. M. Barandiaran, "Ferromagnetic Shape Memory Alloy Actuator for Micro- and Nano-Positioning," *Sensor Letters,* vol. 7, pp. 348-350, Jun 2009.

[16] S. J. Murray, M. A. Marioni, A. M. Kukla, J. Robinson, R. C. O'Handley, and S. M. Allen, "Large field induced strain in single crystalline Ni-Mn-Ga ferromagnetic shape memory alloy," *Journal of Applied Physics,* vol. 87, pp. 5774-5776, May 2000.

[17] K. Ullakko, J. K. Huang, V. V. Kokorin, and R. C. Ohandley, "Magnetically controlled shape memory effect in Ni2MnGa intermetallics," *Scripta Materialia,* vol. 36, pp. 1133-1138, May 1997.

[18] P. Müllner, "Between microscopic and mesoscopic descriptions of twin-twin interaction," *Zeitschrift Fur Metallkunde,* vol. 97, pp. 205-216, Mar 2006.

[19] R. C. Pond and S. Celotto, "Special interfaces: military transformations," *International Materials Reviews,* vol. 48, pp. 225-245, Aug 2003.

[20] J. P. Hirth and R. C. Pond, "Steps, dislocations and disconnections as interface defects relating to structure and phase transformations," *Acta Materialia,* vol. 44, pp. 4749-4763, Dec 1996.

[21] J. M. Howe, R. C. Pond, and J. P. Hirth, "The role of disconnections in phase transformations," *Progress in Materials Science,* vol. 54, pp. 792-838, Aug 2009.

[22] J. Hirth and J. Lothe, *Theory of Dislocations*. New York: McGraw-Hill Book Company, 1968.

[23] J. W. Christian and S. Mahajan, "Deformation Twinning," *Progress in Materials Science,* vol. 39, pp. 1-157, 1995.

[24] R. W. Cahn, "TWINNED CRYSTALS," *Advances in Physics,* vol. 3, pp. 363-445, 1954.

[25] B. A. Bilby and A. G. Crocker, "THEORY OF CRYSTALLOGRAPHY OF DEFORMATION TWINNING," *Proceedings of the Royal Society of London Series a-Mathematical and Physical Sciences,* vol. 288, pp. 240-&, 1965.

[26] P. Müllner and A. H. King, "Deformation of hierarchically twinned martensite," *Acta Materialia,* vol. 58, pp. 5242-5261, Sep 2010.

[27] P. Müllner and A. E. Romanov, "Internal twinning in deformation twinning," *Acta Materialia,* vol. 48, pp. 2323-2337, May 2000.

[28] P. Müllner, A. Geleynse, D. Carpenter, M. Hagler, and M. Chmielus, "Modeling Magnetoplasticity with Disconnections and Disclinations," presented at the Materials Research Society Symposium, 2008.

[29] R. V. Kohn and S. Müller, "Branching of Twins Near an Austenite Twinned-Martenite Interface," *Philosophical Magazine a-Physics of Condensed Matter Structure Defects and Mechanical Properties,* vol. 66, pp. 697-715, Nov 1992.

[30] F. C. Frank and J. H. van der Merwe, "One-Dimensional Dislocations .1. Static Theory," *Proceedings of the Royal Society of London Series a-Mathematical and Physical Sciences,* vol. 198, pp. 205-216, 1949.

[31] D. Hull and D. J. Bacon, *Introduction to Dislocations*, 4 ed. Great Britain: Butterworth and Heinemann, 2001.

[32] A. E. Romanov, "Dislocation and Disclination Structures in Solids," *Physica Scripta,* vol. T49B, pp. 427-429, 1993.

[33] A. E. Romanov, "Screened Disclinations in Solids," *Materials Science and Engineering a-Structural Materials Properties Microstructure and Processing,* vol. 164, pp. 58-68, May 1993.

[34] P. J. Webster, K. R. A. Ziebeck, S. L. Town, and M. S. Peak, "Magnetic Order and Phase-Transformation in NI2MNGA," *Philosophical Magazine B-Physics of Condensed Matter Statistical Mechanics Electronic Optical and Magnetic Properties,* vol. 49, pp. 295-310, 1984.

[35] M. S. Wechsler, D. S. Lieberman, and T. A. Read, "On the Theory of the Formation of Martensite," *Transactions of the American Institute of Mining and Metallurgical Engineers,* vol. 197, pp. 1503-1515, 1953.

[36] J. S. Bowles and J. K. Mackenzie, "The Crystallography of Martensite Transformations .1," *Acta Metallurgica,* vol. 2, pp. 129-137, 1954.

[37] R. C. O'Handley, "Model for strain and magnetization in magnetic shape-memory alloys," *Journal of Applied Physics,* vol. 83, pp. 3263-3270, Mar 1998.

[38] J. Pons, V. A. Chernenko, R. Santamarta, and E. Cesari, "Crystal structure of martensitic phases in Ni-Mn-Ga shape memory alloys," *Acta Materialia,* vol. 48, pp. 3027-3038, Jul 2000.

[39] M. Richard, J. Feuchtwanger, D. Schlagel, T. Lograsso, S. M. Allen, and R. C. O'Handley, "Crystal structure and transformation behavior of Ni-Mn-Ga martensites," *Scripta Materialia,* vol. 54, pp. 1797-1801, May 2006.

[40] N. Lanska, O. Söderberg, A. Sozinov, Y. Ge, K. Ullakko, and V. K. Lindroos, "Composition and temperature dependence of the crystal structure of Ni-Mn-Ga alloys," *Journal of Applied Physics,* vol. 95, pp. 8074-8078, Jun 2004.

[41] V. A. Chernenko, V. L'Vov, J. Pons, and E. Cesari, "Superelasticity in high-temperature Ni-Mn-Ga alloys," *Journal of Applied Physics,* vol. 93, pp. 2394-2399, Mar 2003.

[42] V. A. Chernenko, C. Seguí, E. Cesari, J. Pons, and V. V. Kokorin, "Sequence of martensitic transformations in Ni-Mn-Ga alloys," *Physical Review B,* vol. 57, pp. 2659-2662, Feb 1998.

[43] V. V. Kokorin, V. V. Martynov, and V. A. Chernenko, "Stress - Induced Martensitic Transformation in Ni2MnGa," *Scripta Metallurgica Et Materialia,* vol. 26, pp. 175-177, Jan 1992.

[44] C. Seguí, V. A. Chernenko, J. Pons, and E. Cesari, "Low-temperature-induced intermartensitic phase transformations in Ni-Mn-Ga single crystal," *Journal of Magnetism and Magnetic Materials,* vol. 290, pp. 811-815, Apr 2005.

[45] A. Sozinov, A. A. Likhachev, and K. Ullakko, "Crystal structures and magnetic anisotropy properties of Ni-Mn-Ga martensitic phases with giant magnetic-field-induced strain," *Ieee Transactions on Magnetics,* vol. 38, pp. 2814-2816, Sep 2002.

[46] M. Han, J. C. Bennett, M. A. Gharghouri, J. Chen, C. V. Hyatt, and N. Mailman, "Microstructure characterization of the non-modulated martensite in Ni-Mn-Ga alloy," *Materials Characterization,* vol. 59, pp. 764-768, Jun 2008.

[47] J. Pons, R. Santamarta, V. A. Chernenko, and E. Cesari, "Long-period martensitic structures of Ni-Mn-Ga alloys studied by high-resolution transmission electron microscopy," *Journal of Applied Physics,* vol. 97, Apr 2005.

[48] Z. Nishiyama, *Martensitic Transformations*. New York: Academic Press, 1978.

[49] K. Otsuka, T. Ohba, M. Tokonami, and C. M. Wayman, "New Description of Long-Period Sstacking Order Structures of Martensites in Beta-Phase Alloys," *Scripta Metallurgica Et Materialia,* vol. 29, pp. 1359-1364, Nov 1993.

[50] L. Righi, F. Albertini, G. Calestani, L. Pareti, A. Paoluzi, C. Ritter, P. A. Algarabel, L. Morellon, and M. R. Ibarra, "Incommensurate modulated structure of the ferromagnetic shape-memory Ni2MnGa martensite," *Journal of Solid State Chemistry,* vol. 179, pp. 3525-3533, Nov 2006.

[51] V. A. Chernenko, M. Chmielus, and P. Müllner, "Large magnetic-field-induced strains in Ni-Mn-Ga nonmodulated martensite," *Applied Physics Letters,* vol. 95, Sep 2009.

[52] P. Müllner, D. Makherji, M. Aguirre, R. Erni, and G. Kostorz, "Micromechanics of magnetic-field-induced twin-boundar motion in Ni-Mn-Ga magnetic shape-memor alloys," presented at the TMS (Minerals, Metals, and Materials Society), 2005.

[53] D. B. Williams and C. B. Carter, *Transmission Electron Microscopy*, 2nd ed. vol. Part 3: Imaging: Springer, 2009.

[54] P. Goodhew, J. Humphreys, and R. Beanland, *Electron Microscopy and Analysis*, 3rd ed. New York: Taylor and Francis, 2001.

[55] P. B. Hirsch, A. Howie, and M. J. Whelan, "A Kinematical Theory of Diffraction Contrast of Electron Transmission Microscope Images of Dislcoations and other Defects," vol. 252, Series A. Mathematical and Physical Sciences ed: Philosophical Transactions of the Royal Society of London, 1960, pp. 499-529.

[56] S. Kaufmann, U. K. Rössler, O. Heczko, M. Wuttig, J. Buschbeck, L. Schultz, and S. Fähler, "Adaptive Modulations of Martensites," *Physical Review Letters,* vol. 104, Apr 2010.

[57] V. A. Chernenko, J. Pons, E. Cesari, and K. Ishikawa, "Stress-temperature phase diagram of a ferromagnetic Ni-Mn-Ga shape memory alloy," *Acta Materialia,* vol. 53, pp. 5071-5077, Nov 2005.

[58] D. Hull, "Twinnind Dislocations in Body-Centered Cubic Metals," in *Fifth International Congres for Electron Microscopy*, 1962, pp. B-9.